

# An Imaging Survey for Extrasolar Planets around 45 Close, Young Stars with SDI at the VLT and MMT<sup>1</sup>

Beth A. Biller<sup>1</sup>, Laird M. Close<sup>1</sup>, Elena Masciadri<sup>2</sup>, Eric Nielsen<sup>1</sup>, Rainer Lenzen<sup>3</sup>, Wolfgang Brandner<sup>3</sup>, Donald McCarthy<sup>1</sup>, Markus Hartung<sup>4</sup>, Stephan Kellner<sup>5</sup>, Eric Mamajek<sup>6</sup>, Thomas Henning<sup>3</sup>, Douglas Miller<sup>1</sup>, Matthew Kenworthy<sup>1</sup>, and Craig Kulesa<sup>1</sup>

bbiller@as.arizona.edu

<sup>1</sup> *Steward Observatory, University of Arizona, Tucson, AZ 85721*

<sup>2</sup> *Observatorio Astrofisico di Arcetri, L.go E. Fermi 5, 50125 Florence, Italy*

<sup>3</sup> *Max-Planck-Institut für Astronomie, Königstuhl 17, 69117 Heidelberg, Germany*

<sup>4</sup> *European Southern Observatory, Alonso de Cordova 3107, Santiago 19, Chile*

<sup>5</sup> *W.M. Keck Observatory, 65-1120 Mamalahoa Hwy., Kamuela, HI 96743*

<sup>6</sup> *Harvard-Smithsonian Center for Astrophysics, 60 Garden St., Cambridge, MA 02138*

## ABSTRACT

We present the results of a survey of 45 young ( $\lesssim 250$  Myr), close ( $\lesssim 50$  pc) stars with the Simultaneous Differential Imager (SDI) implemented at the VLT and the MMT for the direct detection of extrasolar planets.<sup>1</sup> As part of the survey, we observed 54 objects total, of which 45 were close, young stars, 2 were somewhat more distant ( $< 150$  pc), very young ( $\leq 10$  Myr) stars, 3 were stars with known radial velocity planets, and 4 were older, very nearby ( $\leq 20$  pc) solar analogues. Our SDI devices use a double Wollaston prism and a quad filter to take images simultaneously at 3 wavelengths surrounding the  $1.62 \mu\text{m}$  methane absorption bandhead found in the spectrum of cool brown dwarfs and gas giant planets. By performing a difference of adaptive optics corrected images in these filters, speckle noise from the primary star can be significantly attenuated, resulting in photon (and flat-field) noise limited data. In our VLT data, we achieved H band contrasts  $\gtrsim 10$  mag ( $5\sigma$ ) at a separation of  $0.5''$  from the primary star on 45% of our targets and H band contrasts of  $\gtrsim 9$  mag at a separation of  $0.5''$  on

---

<sup>1</sup>based on observations made with the MMT and the ESO VLT at Paranal Observatory under programme ID's 074.C-0548, 074.C-0549, and 076.C-0094

80% of our targets. With this degree of attenuation, we should be able to image ( $5\sigma$  detection) a  $5 M_{Jup}$  planet 15 AU from a 70 Myr K1 star at 15 pc or a  $5 M_{Jup}$  planet at 2 AU from a 12 Myr M star at 10 pc. Our 45 southern targets were observed with the VLT while 11 of our northern targets were observed with the MMT (2 objects were observed at both telescopes). We believe that our SDI images are the highest contrast astronomical images ever made from ground or space for methane rich companions  $\leq 1''$  from their star. We detected no tentative candidates with  $S/N > 2\sigma$  which behaved consistently like a real object. Followup observations were conducted on 8  $< 2\sigma$  candidates (with separations of 3 - 15.5 AU and masses of 2-10  $M_{Jup}$ , had they been real) – none of which were detected at a second epoch. In the course of our survey, we also discovered 5 new close stellar binary systems with measured separations of 0.14'' to 0.26''. For the best 20 of our survey stars, we attained 50%  $5\sigma$  completeness for 6-10  $M_{Jup}$  planets at semi-major axes of 20-40 AU. Thus, our completeness levels are sufficient to significantly test theoretical planet distributions. From our survey null result, we can rule out (at the 98% confidence/ $2.0\sigma$  level) a model planet population using a planet distribution where  $N(a) \propto \text{constant}$  out to a distance of 45 AU (further model assumptions discussed within).

*Subject headings:* planets: extrasolar — instrumentation: adaptive optics — binaries: general

## 1. Introduction

While over 200 extrasolar planets have been detected<sup>2</sup> over the last 11 years (mostly via the radial velocity technique), very few extrasolar planet candidates have been imaged directly (for instance, 2MASS 1207b ( $\sim 8 \pm 3 M_{Jup}$ ), Oph 1622B ( $\sim 13 \pm 5 M_{Jup}$ ), and CHXR 73 B ( $\sim 12.5 \pm 8 M_{Jup}$ ) Chauvin et al. 2005a; Close et al. 2007a; Luhman et al. 2006; Brandeker et al. 2006). The few candidates discovered of “planetary mass”  $< 13 M_{Jup}$  are companions to brown dwarfs and possess properties more similar to young brown dwarfs (separations  $> 50$  AU; surface gravity  $g \gtrsim 0.3$ ) than to giant extrasolar planets orbiting sun-like stars. Based on their large ( $> 50$  AU) separations, these objects appear to have formed via a fragmentation process, more similar to brown dwarfs. Hence, to date no true images of extrasolar planets have been obtained.

---

<sup>2</sup><http://exoplanet.eu/catalog.php>, maintained by Jean Schneider

Theoretically, a large telescope ( $D > 6$  meters) plus an adaptive optics (AO) system should be able to reach the photon-noise limit at  $1''$  separations from the star with an hour of exposure time and thus attain the very high ( $>10^5$ ) contrasts necessary to image a young extrasolar giant planet. Thus, numerous adaptive optics surveys to directly detect extrasolar planets have been completed (for instance, Kaisler et al. 2003; Masciadri et al. 2005). These surveys have yielded interesting contrast limits but no true extrasolar giant planet candidates.

The difficulty in directly imaging extrasolar giant planets can be attributed to the unfortunate fact that bright quasi-static speckles (also known as super speckles) caused by slowly evolving instrumental aberrations remain in adaptive optics images even after adaptive optics correction (see for example Racine et al. 1999). These super speckles evolve stochastically on relatively long (minute) timescales and also vary somewhat chromatically, producing correlated speckle noise which is very difficult to calibrate and remove (Racine et al. 1999). For photon-noise limited data, the signal to noise S/N increases as  $t^{0.5}$ , where  $t$  is the exposure time. Approximately speaking, for speckle-noise limited data, the S/N does not increase with time past a specific speckle-noise floor (limiting AO contrasts often to  $\sim 10^3$  at  $0.5''$ , Racine et al. 1999; Masciadri et al. 2005). More exactly, S/N does continue to increase with time, but as the speckle noise in successive frames becomes correlated, the N gain becomes considerably slower. Effectively independent exposures then have durations of many minutes rather than a small fraction of a second (Racine et al. 1999). This correlated speckle noise is considerably above the photon noise limit and makes planet detection very difficult. Interestingly, space telescopes such as HST also suffer from limiting correlated speckle noise due to temperature variations which induce changes in the PSF (known as “breathing”, Schneider et al. 2003).

Many observatories, including Gemini, Subaru, and the VLT, are currently building dedicated planet-finding AO/coronagraph cameras in order to overcome this speckle noise floor (Dohlen et al. 2006; Macintosh et al. 2006; Tamura & Lyu 2006). A number of instrumental speckle-attenuation methods have been proposed, such as spectral differential imaging (Racine et al. 1999; Marois et al. 2000, 2002, 2005), azimuthal differential imaging (Marois et al. 2006), integral field spectroscopy (Sparks & Ford 2002; Berton et al. 2006; Thatte et al. 2007), precise wavelength control methods such as those developed at the High Contrast Imaging Testbed (Trauger et al. 2004), focal plane wavefront sensing (Codona & Angel 2004; Kenworthy et al. 2006), and nulling interferometry (Liu et al. 2006).

The Simultaneous Differential Imagers at the VLT and MMT, built and commissioned by our team (Lenzen et al. 2004, 2005; Close et al. 2005a), utilizes a spectral differential speckle-attenuation technique (pioneered by Racine et al. 1999; Marois et al. 2000, 2002, 2005). It

exploits a methane absorption feature at  $1.62 \mu\text{m}$  (see Fig. 1) which is robustly observed in substellar objects with spectral type later than T3.5 (Geballe et al. 2002; Burrows et al. 2001). SDI utilizes specialized hardware to image simultaneously inside and outside this methane feature with custom 25 nm filters (see Fig. 1). Since the super-speckles are coherent with the starlight and both starlight and speckles have a flat spectrum (see Fig. 1) in this narrow wavelength band ( $\delta\lambda / \lambda \simeq 1.6\%$ ), subtracting the “on” and “off” methane absorption images removes the starlight and its speckles, while preserving light from any substellar methane companion to the star.

We have completed a 54 star survey with the SDI device at the VLT and MMT. Survey stars were chosen primarily according to proximity to the Sun ( $\lesssim 50$  pc) and youth ( $\lesssim 300$  Myr, typically  $< 100$  Myr). We observed 47 young ( $\lesssim 250$  Myr) stars, 3 nearby stars with known RV planets, and 4 very close ( $\lesssim 20$  pc) older solar analogues. We obtained contrasts of  $\Delta H > 10$  mag ( $5 \sigma$ ) at  $0.5''$  for 45% of target objects at the VLT and contrasts of  $\Delta H > 9$  mag ( $5 \sigma$ ) at  $0.5''$  for 80% of our targets. The VLT SDI device is fully commissioned and available to the community and the MMT SDI device is a PI instrument with the ARIES camera. In contrast, the dedicated planet-finding instruments such as Sphere and GPI (Dohlen et al. 2006; Macintosh et al. 2006) being built at the VLT and Gemini will not see first light for several years. Thus, as a precursor to planet surveys with these dedicated planet finding cameras, the results from the SDI devices are especially timely and relevant, particularly to inform the large Gemini NICI survey starting in 2007 (Liu et al. 2005).

## 2. The Simultaneous Differential Imagers at the VLT and MMT

The VLT Simultaneous Differential Imager (henceforth SDI) was built at the University of Arizona by L. Close and installed in a special f/40 camera relay for the VLT AO camera CONICA built by R. Lenzen at the Max Planck Institute for Astronomy, Heidelberg. These were both installed at the VLT in August 2003. The MMT SDI was also built at the University of Arizona. In February 2004, it was installed in the ARIES f/30 camera built by D. McCarthy. Both devices are available to the observing communities of their respective telescopes.

### 2.1. Hardware Considerations

The SDI device consists of a custom double Wollaston, which splits the incoming AO beam into 4 identical beams (utilizing calcite birefringence to minimize non-common path

error – adding only  $\lesssim 10$  nm rms of differential non-common path errors per the first few Zernikes modes – Lenzen et al. 2004a). Each beam then passes through a narrowband filter with a central wavelength either on or off methane absorption. Three different filters were used; all filters were placed in different quadrants on the same substrate. SDI filters for the VLT and MMT were manufactured by Barr Associates. Filter wavelengths were chosen on and off the methane absorption feature at  $1.62 \mu\text{m}$  and were spaced closely (every  $0.025 \mu\text{m}$ ) in order to limit residuals due to speckle and calcite chromatism. We used four filters F1, F2, F3a, and F3b with measured cold central wavelengths  $F1 \equiv 1.575 \mu\text{m}$ ,  $F2 \equiv 1.600 \mu\text{m}$ , and  $F3a \equiv F3b \equiv 1.625 \mu\text{m}$ . The filters are approximately  $0.025 \mu\text{m}$  in bandwidth (1.6%). The SDI filter transmission curves overlaid on a theoretical young planet spectrum (private communication, D. Sudarsky) are presented in Fig. 1.

## 2.2. Discoveries with the SDI Cameras

The SDI device has already produced a number of important scientific results: the discovery of the important calibrator object AB Dor C (Close et al. 2005b) which is the tightest ( $0.16''$ ) low mass ( $0.090 \pm 0.05 M_{\odot}$ ,  $\sim 100\times$  fainter) companion detected by direct imaging, the most detailed methane surface maps of Titan from the pre-Cassini era (Hartung et al. 2004), the discovery of  $\epsilon$  Ind Ba and Bb, the nearest binary brown dwarf (McCaughrean et al. 2004), the discovery of SCR 1845-6357B, a very close ( $3.85$  pc) T6 brown dwarf (Biller et al. 2006b), and evidence of orbital motion for Gl 86B, the first known white dwarf companion to an exoplanet host star (Mugrauer & Neuhauser 2005). In fact, the SDI device discovered all known brown dwarfs within 5 pc of the Sun. It has also set the best upper limit on the luminosity of the older ( $\sim 1$  Gyr) extrasolar planet around  $\epsilon$  Eri.

## 2.3. Observational Techniques and Data Reduction

To ensure the highest possible signal to noise ratio and to maximize SDI speckle attenuation, a complex data acquisition procedure was followed for each star. For each object observed, we saturated the inner  $\sim 0.1''$  of the star, thus providing a wide dynamic range and contrast down into the halo. Base exposure times (DIT) range from 0.3 to 20 s (typically this was  $> 2$  s to allow Fowler sampling at the VLT), depending on the H magnitude of the observed star. A number of exposures (NDIT) with the base exposure time are then coadded in hardware to produce a standard  $\sim 2$  minute long base datum. An example raw datum is

presented in Fig. 2<sup>3</sup>.

Base datum are then taken at a grid of dither positions ( $4 \times 0.5''$  spacings with the MMT,  $5 \times 0.5''$  spacings with the VLT). This dither pattern is then repeated at typically 2 telescope “roll angles” (where a “roll angle” refers to a different field derotator position / position angle (henceforth PA) settings). A subtraction of data taken at different roll angles further attenuates super-speckle residuals (since the weak residual speckles after SDI subtraction are instrumental features in the SDI optics which do not shift with a change in roll angle) while producing a very important signature “jump” in position for any physical companion (since a physical companion will appear to shift by the roll angle difference between datasets). For a space telescope such as Hubble (where the entire telescope can be rolled), a companion detected at the  $5\sigma$  level in two different roll angles would be detected at the  $7\sigma$  level (a S/N gain of  $\sim \sqrt{2}$ ) across the entire dataset (assuming roughly Gaussian statistics). This method is somewhat less effective with ground based telescopes where field rotation is provided by the field derotator rather than rolling the entire telescope (thus, super speckles from the telescope optics can appear to rotate by the roll angle as well). Nonetheless, observing at two roll angles provides us with two independent detections of a substellar companion at different locations on the detector, thus allowing us to rule out a “false positive” detection at an extremely high level of confidence – indeed, the only 3 faint companions ( $\epsilon$  Ind Bb, SCR 1845-6357B, and AB Dor C) ever detected with  $\geq 5\sigma$  using SDI in more than one roll angle have *all proven to be real*. A typical observing block at the VLT then consists of the following series of : 1)  $\sim 10$  minute long dither pattern taken with a roll angle of 0 degrees. 2)  $\sim 10$  minute long dither pattern taken with a roll angle of 33 degrees. 3)  $\sim 10$  minute long dither pattern taken with a roll angle of 33 degrees. 4)  $\sim 10$  minute long dither pattern taken with a roll angle of 0 degrees. A custom template was developed at the VLT to automate this process in each OB.

Each base datum was reduced using a custom IDL pipeline (described in detail in Biller et al. (2006a) and Biller et al. (2006c)). This pipeline performs sky-subtraction, flat-fielding, and bad pixel removal, extracts a square aperture around each separate filter image, scales the platescale of each filter image so that the speckles in each filter fall at the same radii despite chromatic differences, scales the flux in each image to remove any quantum efficiency differences between the images, and filters out very low ( $>15$  pixels) spatial frequencies by unsharp masking each image. Each filter image is then initially aligned to a reference image

---

<sup>3</sup>As with all our survey data, this was taken with the original SDI double Wollaston prism. In February 2007, the original prism was replaced with a next generation prism which is cut in such a way that each subimage now subtends a whole quadrant of the detector chip. The new prism is also fabricated from YV04, a material which produces smaller chromatic errors at  $1.6\mu\text{m}$  than the original calcite.

to within 0.25 pixels using a custom shift and subtract algorithm (Biller et al. (2006a,c)). One master reference image is used for each  $\sim 40$  minute long dataset. After each of the filter images has been aligned to the reference image, we calculate 2 differences which are sensitive to substellar companions of spectral types T ( $T_{eff} < 1200$  K) and “Y” ( $T_{eff} < 600$  K). The first is optimal for T spectral types:

$$Difference1 = F1(1.575 \mu m) - F3a(1.625 \mu m) \quad (1)$$

The second is optimal for Y spectral types:

$$Difference2 = F2(1.6 \mu m) - F3a(1.625 \mu m) \quad (2)$$

An additional alignment is performed before the SDI subtraction; using the F1 image as our reference image, we align images F1 and F3a to within 0.05 pixels. A similar alignment is performed with images F2 and F3a, using the F2 image as the reference image.

These differences are also somewhat sensitive to hotter substellar companions (L and early T spectral types), due to the fact that the platescale in each filter image has been scaled to a reference platescale to align the Airy patterns in each image. A real object (as opposed to a speckle) will not scale with the Airy pattern and thus, after scaling, will appear at a slightly different radius in each filter image. Subtracting images in different filters will then produce a characteristic dark-light radial pattern for a real object. This effect obviously scales with radius – at the VLT, an object at 0.5” will be offset by less than 1 pixel between filters, while an object at 1.5” will be offset by  $\sim 3$  pixels, producing a very noticeable pattern. Thus, the SDI subtractions have a limited sensitivity to bright L and early T companions. We note that AB Dor C ( $\Delta H \sim 5$  mag) was detected at 0.15” (February 2004, Close et al. 2005) and 0.2” (September 2004, Nielsen et al. 2005) separations from AB Dor A even though AB Dor C has no methane absorption features (as is expected from its M5.5 spectral type, Close et al. 2007b.)

We additionally calculate one further non-differenced combination sensitive to M, L, and early T companions:

$$Broadband = F1(1.575\mu m) + F2(1.6\mu m) + F3(1.625\mu m) \quad (3)$$

After each datum is pipelined the data are further processed in IRAF. For each  $\sim 10$  minute long dither pattern, all three combinations described above and the four reduced filter images are median combined. Each 10 minute dataset is then differenced with the

following 10 minute dataset (taken at a different position angle). All roll-angle differenced images for each target object observation are then median combined to produce the final data product.

A fully reduced  $\sim 30$  minute dataset of AB Dor A (70 Myr K1V star at a distance of 14.98 pc,  $V=6.88$ ) from the VLT SDI device is presented in Fig. 3. Simulated planets have been added at separations of 0.55, 0.85, and 1.35" from the primary, with  $\Delta F1(1.575\mu\text{m}) = 10$  mag (attenuation in magnitudes in the 1.575  $\mu\text{m}$  F1 filter) fainter than the primary. For details and further discussion of these planet simulations see Section 3.4.

### 3. The SDI Survey

#### 3.1. Survey Design / Target Selection

Survey objects were selected primarily on the basis of youth and proximity. With a number of exceptions, our 54 survey objects are within 50 pc of the Sun and less than 250 Myr in age. (The 9 exceptions include three somewhat older stars with known radial velocity planets, 2 more distant ( $<150$  pc) stars with extreme youth indicators, and 4 older nearby young solar analogues which were initially misclassified as young objects.) Distances were obtained for 48 of our objects from Hipparcos parallax measurements (parallaxes of  $>0.02''$ , corresponding to distances  $<50$  pc, Perryman et al. 1997). Stars were age-selected according to two methods: 1) if possible, according to young cluster membership (and adopting the established age for that cluster) for clusters with well established ages such as the Beta Pic, TW Hya, AB Dor and Tuc-Hor moving groups or 2) according to other age indicators including the strength of spectral age indicators (for instance, the Li 6707, the Calcium H and K lines, and  $H\alpha$  emission) as well as from X-ray emission, variability, and rotational speed. As moving group ages are generally more robust than measurements for individual stars, we expect the ages of stars in these associations, on average, to have greater accuracy. Our survey covers stars in the Beta Pic, TW Hya, AB Dor, IC 2391, and Tucanae/Horologium moving groups.

We select targets stars based on two overlapping criteria: 1) stars within 25 pc and younger than 250 Myr, and 2) stars within 50 pc and younger than 40 Myr (see Fig. 4). Our original list has been modified according to the amount of allocated time at the telescope, the unavailability of GTO targets, as well as severe weather constraints for the MMT portion of our survey. At the VLT, our observing runs spanned the months of August through February over 2004 and 2005. Thus, due to the spacing of observing runs, in the south, the survey is close to complete from  $\sim 17$  -  $\sim 13$  hours RA. At the MMT, we had two observing runs, one



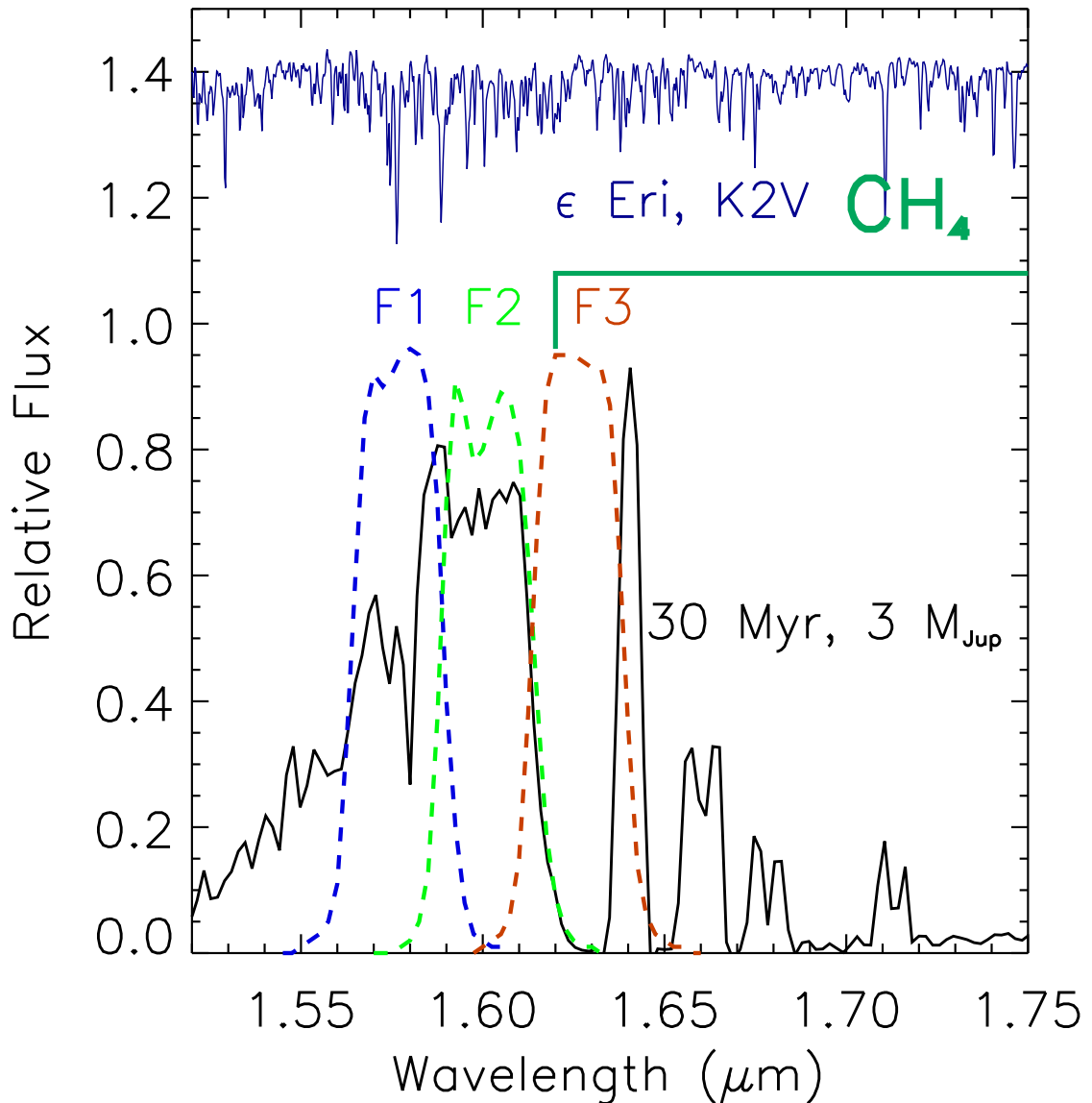


Fig. 1.— SDI filter transmission curves overlaid on the theoretical spectrum (private communication, D. Sudarsky) of a young extrasolar planet (30 Myr, 3  $M_{Jup}$ ). Filters 1 and 2 sample off the 1.62  $\mu\text{m}$   $\text{CH}_4$  absorption feature, while filter 3 samples within the absorption feature. In contrast, the spectrum of the K2V star  $\epsilon$  Eri (Meyer et al. 1998) is flat across the whole wavelength band. Subtracting images taken in filters “on” and “off” the methane absorption feature will remove the star and speckle noise (which is coherent with the starlight) while preserving any light from giant planet companions. (Details of the complex SDI data pipeline are provided in Section 2.3.)

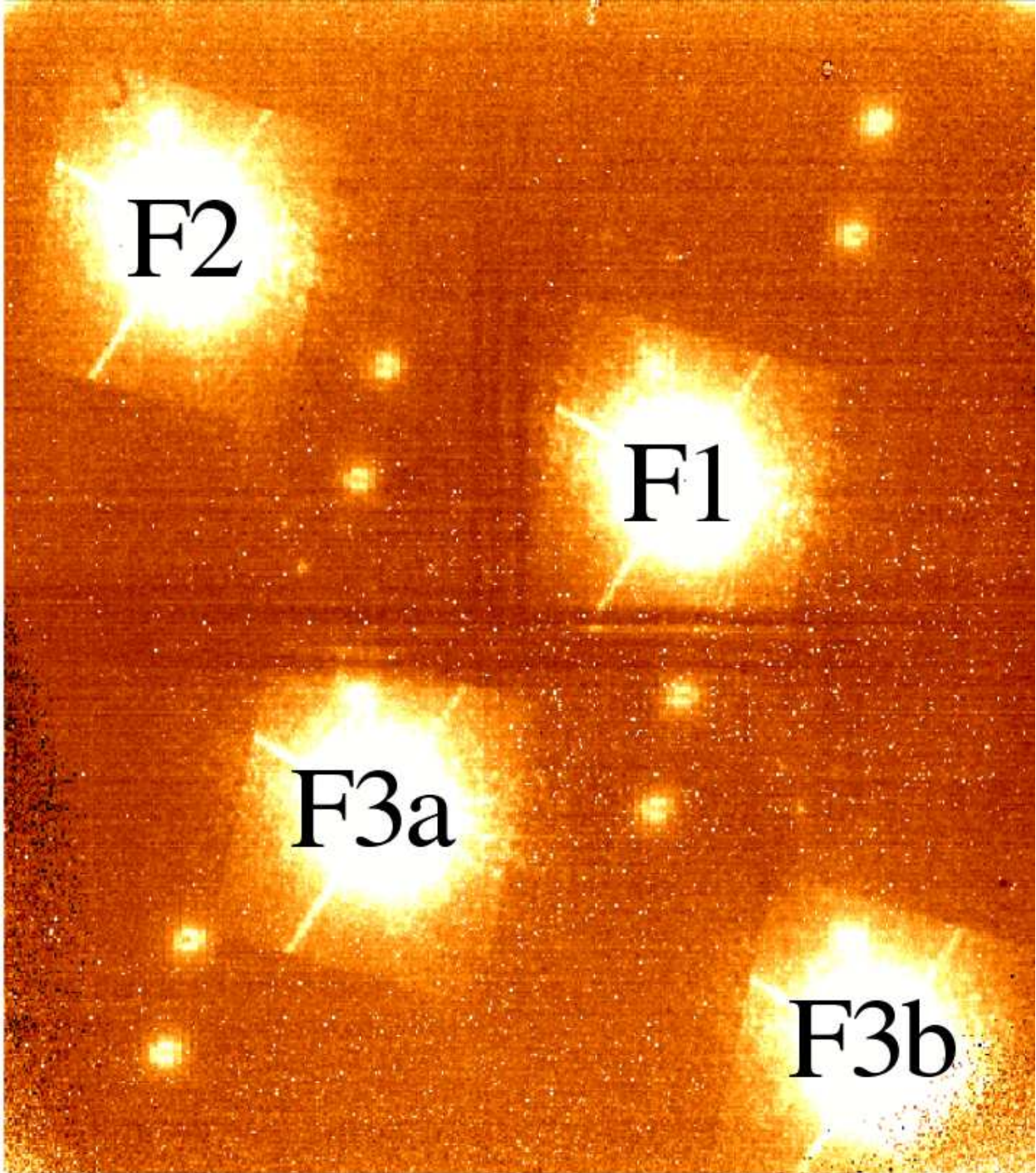


Fig. 2.— Two minutes of raw SDI data from NACO SDI’s  $1024 \times 1024$  Aladdin array in the VLT CONICA AO camera (Lenzen et al. 2004). A number of electronic ghosts are apparent outside the four square filter apertures (each aperture is rotated by  $30^\circ$ ); indeed, filter apertures were specifically selected to exclude these ghosts. Note that this is an image of the original Alladin array; the current SDI array has far fewer bad pixels.

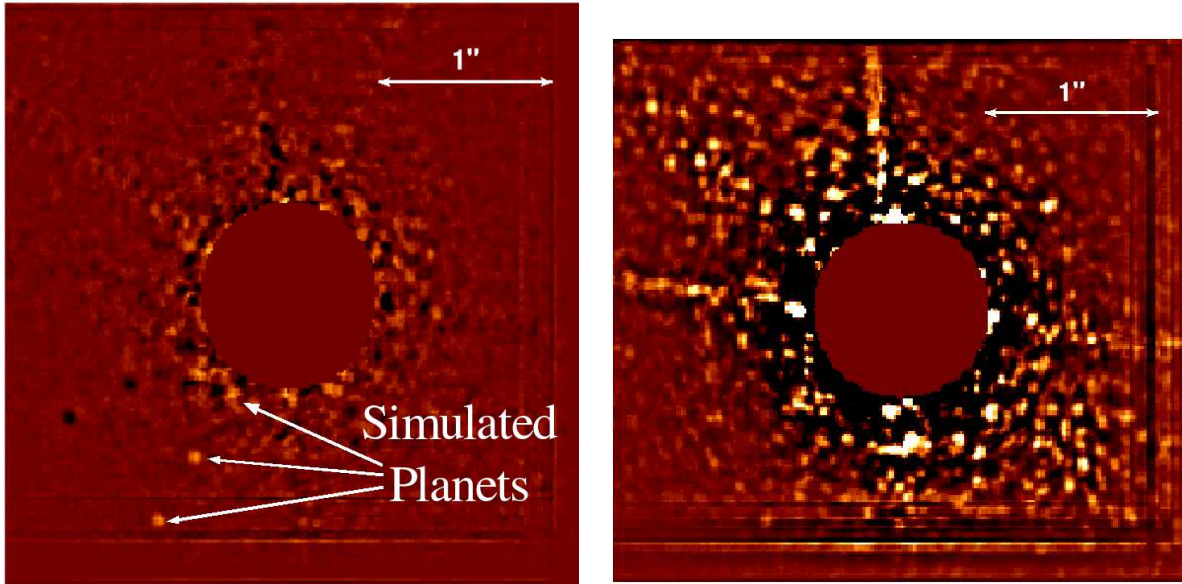


Fig. 3.— **Left:** A complete reduced dataset (28 minutes of data at a series of rotator angles (“roll angles”) –  $0^\circ$ ,  $33^\circ$ ,  $33^\circ$ ,  $0^\circ$ ) from the VLT SDI device. Simulated planets have been added at separations of 0.55, 0.85, and 1.35” from the primary, with  $\Delta F1(1.575\mu\text{m}) = 10$  mag (star-planet contrast in magnitudes) fainter than the primary. These planets are scaled from unsaturated images of the example star (AB Dor A) taken right before the example dataset (and have fluxes and photon noise in each filter appropriate for a T6 effective temperature). Past 0.7”, the simulated planets are detected in both roll angles with  $S/N > 10$ . Observing at two different roll angles produces two independent detections, and hence makes the chance of detecting a “false positive” almost null. **Right:** Standard AO data reduction of the same dataset. Filter images have been coadded (rather than subtracted), flat-fielded, sky-subtracted, and unsharp-masked. Simulated planets have been added with the same properties and at the same separations as before. None of the simulated planets are clearly detected in the standard AO reduction. Additionally, many more bright super speckles remain in the field.

in May 2005 and one in February 2006. Thus, in the north, the survey is complete for the RA range 11 - 21 hours.

Survey objects are presented in Table 1. A detailed table of observations is presented in Table 2. Survey objects are plotted as a function of distance and age in Fig. 4. Our “median” survey object is a K star with an age of 30 Myr and at a distance of 25 pc.

### 3.2. The Performance of the SDI Filters as Spectral Indices

It is important to carefully consider the expected strength of the 1.62  $\mu\text{m}$  methane absorption break utilized by the SDI device. The stronger the break strength, the more companion light is preserved after SDI filter subtraction. For a candidate object with a weak break strength, SDI subtraction may effectively attenuate the candidate object itself, rendering it undetectable (although, at separations  $> 0.15''$ , a bright object may still be detectable due to the characteristic dark-light radial pattern produced by any real object after pipelining, see Section 2.2.)

To determine the methane break strength expected for a candidate object (and thus, the expected performance of SDI for that candidate), we define an SDI methane spectral index calculated from our SDI F1(1.575  $\mu\text{m}$ ) and F3(1.625  $\mu\text{m}$ ) filter images (similar to the methane spectral index defined by Geballe et al. 2002).

$$index\left(\frac{F1}{F3}\right) = \frac{\int_{\lambda_1=1.5625\mu\text{m}}^{\lambda_2=1.5875\mu\text{m}} S_\lambda F1(\lambda) d\lambda}{\int_{\lambda_3=1.6375\mu\text{m}}^{\lambda_4=1.6125\mu\text{m}} S_\lambda F3(\lambda) d\lambda} \quad (4)$$

Each SDI filter was manufactured by Barr Associates to have a precise bandwidth of 0.025  $\mu\text{m}$ , so the wavelength intervals ( $\lambda_2 - \lambda_1 = \Delta\lambda = \lambda_4 - \lambda_3$ ) in the numerator and denominator have the same length for the SDI methane index.

We calculated SDI spectral indices for the four brown dwarfs which have been observed with SDI – the T6 Gl 229B (Nakajima et al. 1995), the T5.5 SCR 1845B (Biller et al. 2006b) and  $\epsilon$  Ind Ba-Bb (T6 + T1) (McCaughrean et al. 2004). Since we only possess SDI data on a limited number of T dwarfs, we calculated the same SDI spectral indices from spectra of 56 L dwarfs and 35 T dwarfs (Knapp et al. 2004) in order to evaluate the performance of the SDI for a wide range of L and T dwarf objects. Spectra for these objects were obtained from Sandy Leggett’s L and T dwarf archive <sup>4</sup>. In order to make an accurate comparison, SDI

---

<sup>4</sup><http://www.jach.hawaii.edu/~skl/LTdata.html>

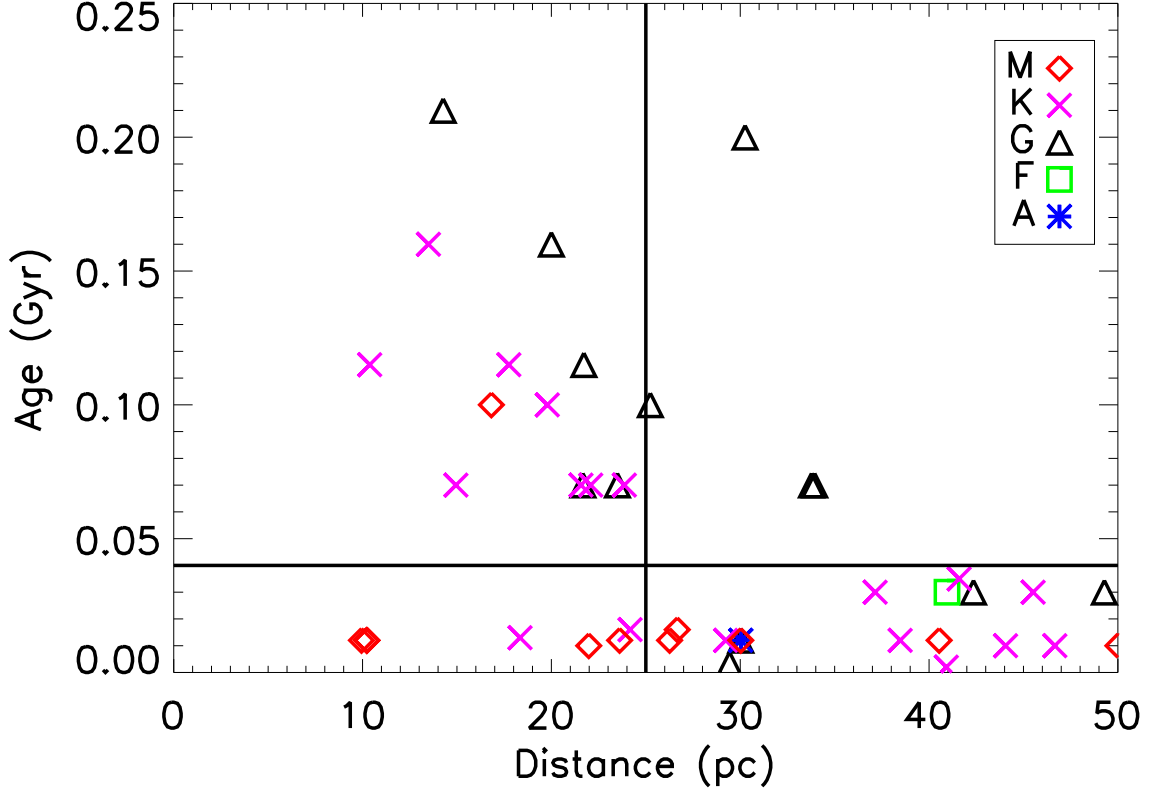


Fig. 4.— Age vs. distance for our survey stars. Spectral types are delineated by plot symbols. Objects were selected according to youth and proximity to the Sun. 45 of our survey objects are within 50 pc of the Sun and less than 250 Myr in age. Of the remaining objects, 2 are very young ( $<10$  Myr), somewhat more distant ( $<150$  pc) objects, 3 are nearby stars with known RV planets, and 4 are nearby solar analogues ( $<20$  pc) that were initially misclassified as young. We selected targets according to two overlapping criteria (shown on plot as solid black lines) 1) stars within 25 pc and younger than 250 Myr and 2) stars within 50 pc and younger than 40 Myr. Stars were age-selected according to association membership, or, in the case of unassociated stars, age indicators such as the strength of the Li 6707 Å line, Calcium H and K lines, H  $\alpha$  emission, X-ray emission, etc. Distances were obtained from Hipparcos parallax measurements (parallaxes of  $>0.02''$ ). Our “median” survey object is a K star with an age of 30 Myr and at a distance of 25 pc.

filter transmission curves were convolved into these calculations (see Fig. 1). Since we have full spectral data for these objects, we also calculated the  $1.62 \mu\text{m}$  methane spectral index defined by Geballe et al. (2002), which were found to be similar to our SDI methane spectral indices. SDI methane spectral indices are plotted for both the M9 and T6 components of SCR 1845, the T dwarfs Gl 229B,  $\epsilon$ Ind Ba,  $\epsilon$ Ind Bb, and 94 other L and T dwarfs in Fig. 5. Geballe et al. (2002) note that Gl 229B has an anomalously high methane index for its spectral type and assign a large uncertainty to Gl 229B’s spectral type –  $T6 \pm 1$  – which is also reflected in its anomalously large SDI spectral index compared to other T6 dwarfs. From this analysis, we conclude that the SDI device can effectively detect objects with spectral type later than T3. Since T dwarfs with spectral type earlier than T3 are relatively uncommon compared to later T dwarfs, the SDI device can effectively detect the full range of extrasolar giant planet / brown dwarf spectral types of interest. According to the models of Burrows et al. 2003 and Marley et al. 2006, planets  $>10$  Myr old should possess  $T_{\text{eff}} < 800$  K and have spectral type of T8 or greater.

### 3.3. Contrast Limits and Minimum Detectable Planet Separation

To determine the range of possible star-planet contrasts achieved in our survey, we generated noise curves as a function of radius for every survey star. We tested three different methods of generating noise curves: 1) translating a  $6 \times 6$  pixel ( $0.1'' \times 0.1''$ ) box along a particular radial trajectory away from the center of the star image (typical PSF FWHM was 3-5 pixels) then calculating the standard deviation in the box at each point along this trajectory, 2) averaging noise curves generated along four such trajectories, and 3) calculating the standard deviation within annular regions 6 pixels in width centered on the primary PSF (spider diffraction spikes were not masked out in this case because they are already well removed by the spectral difference). Noise curves generated in these three manners are presented for a set of 6 typical program stars (AB Dor, DX Leo, GJ 182, AB Pic, GJ 799A, and GJ 799B) in Fig. 6. In general, all three methods produce remarkably similar noise curves and are equally suitable for characterizing the noise properties of an observation. However, we choose to utilize the single trajectory method because it best simulates the particular signal to noise issues encountered when searching for faint companions among super-speckles of similar intensity and FWHM (since it preserves pixel to pixel noise variations due to super-speckles). The annular method averages out speckle noise properties azimuthally. This produces somewhat unrealistic results in the case of a faint companion search where one is concerned only with the speckle structure within the local area of a candidate faint companion – speckle structure on the other side of the image is unimportant. In addition, we have tried to choose very “typical” trajectory per star – ideally, trajectory to trajectory

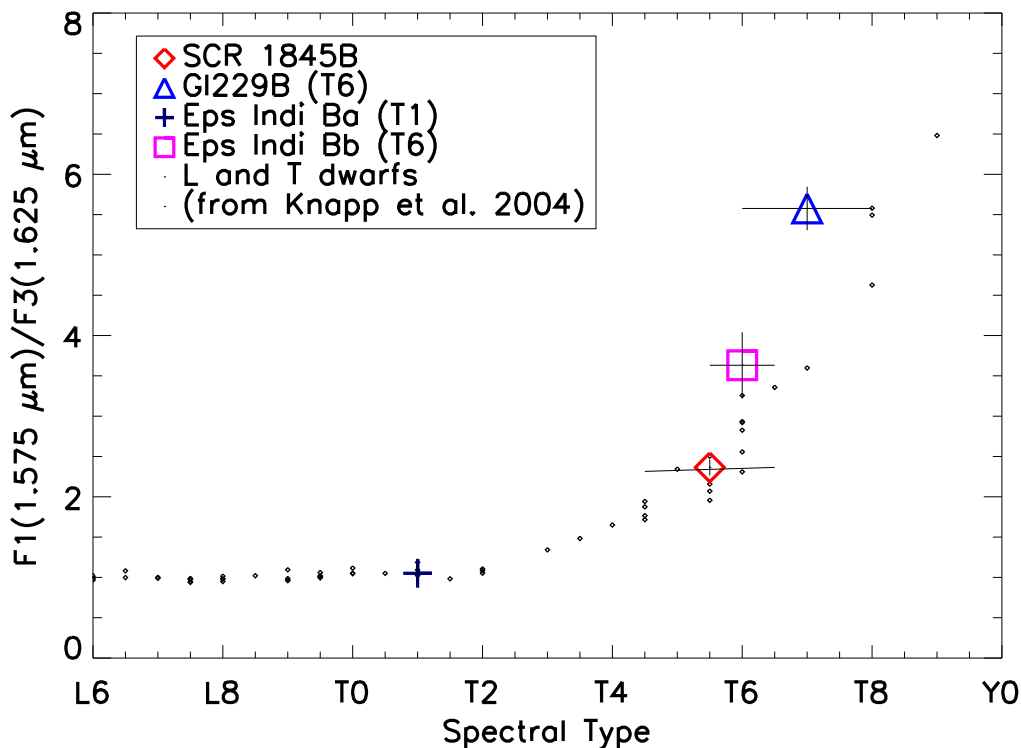


Fig. 5.— SDI methane spectral indices for the T dwarfs SCR 1845B, Gl 229B,  $\epsilon$  Ind Ba, and  $\epsilon$  Ind Bb (from Biller et al. 2006b). As a comparison, SDI methane spectral indices calculated from spectra for 94 L and T dwarfs (spectra from Knapp et al. 2004) are overplotted. SCR 1845B, Gl 229B, and  $\epsilon$  Ind Bb show strong methane indices, whereas  $\epsilon$  Ind Bb (T1) is relatively constant in flux across the SDI filters and has a much lower methane index. Geballe et al. (2002) note that Gl 229B has an anomalously high methane index for its spectral type. While Geballe et al. (2002) find an overall spectral type of  $T6 \pm 1$  for Gl 229B, they assign Gl 229B a spectral type of T7 based on the methane index (which we adopt here).

variations will average out across the entire survey.

Noise curves for each program star were calculated along a trajectory  $45^\circ$  from the image x axis in the first quadrant. The  $45^\circ$  was selected as one of many possible representative trajectories which was unaffected by instrumental effects such as spider arms, vibrations along azimuth or altitude mounts, etc. At each point along this trajectory, the standard deviation was calculated (except for the PSF noise curve, for which the mean was calculated).

A fully labeled example noise curve for the star DX Leo is presented in Fig. 7. Noise curves were generated for a number of cases for each object. First, a noise curve was generated for the full reduced and differenced SDI data (labeled SDI data curve) (F1(1.575  $\mu\text{m}$ ) - F3a(1.625  $\mu\text{m}$ ) for two roll angles). A PSF noise curve curve was generated from a median combination of all the F1(1.575  $\mu\text{m}$ ) filter images for each dataset weighted according to the number of exposures, dithers, and roll angles in the dataset. To recreate the equivalent observation without using the SDI technique (and thus characterize the performance of SDI compared to conventional AO techniques), an “optimized conventional AO” curve was generated by combining images from all three filters at each roll angle:

$$Broadband = F1(1.575\mu\text{m}) + F2(1.6\mu\text{m}) + F3(1.625\mu\text{m}) \quad (5)$$

then unsharp masking to remove low spatial frequencies, and subtracting the “Broadband” combinations at different roll angles from each other.

To characterize the noise level in each observation, we calculated an SDI noise curve, which is a combination of photon-noise, flat-field noise, and read noise. Per exposure:

$$\sigma_{SDI} = \sqrt{\sigma_{photon}^2 + \sigma_{flatfield}^2 + \sigma_{readnoise}^2} \quad (6)$$

Photon-noise was calculated as:

$$\sigma_{photon} = \sqrt{n_{electrons}} \quad (7)$$

Readout noise for the CONICA detector at the VLT in Fowler sampling mode is 1.3 ADU (analog-to-digital unit). The gain for the latest CONICA detector in the Fowler sampling mode is 12.1 electrons/ADU so  $\sigma_{readnoise} = 15.73$  electrons.

NACO and ARIES flat fields were found to be accurate to about 1%, so flat-field noise was estimated as:



$$\sigma_{flatfield} = \epsilon n_{electrons} \quad (8)$$

where  $\epsilon=0.01$ . The total noise for a full observation (4-5 dithers, 2-4 roll angles) was then calculated by weighting the SDI noise per exposure by the number of exposures (NDIT  $\times$  number of dithers  $\times$  number of roll angles):

$$\sigma_{SDI\_fullobs} = \sigma_{SDI} \sqrt{NDIT \times (\text{number of dithers}) \times (\text{number of roll angles})} \quad (9)$$

The PSF curve for a full observation was similarly weighted:

$$PSF = (\text{medianPSF}) \times NDIT \times (\text{number of dithers}) \times (\text{number of roll angles}) \quad (10)$$

For the sample curve shown in Fig. 7, the SDI data is “flat-field” limited within 0.5” of the star. From 0.5” onwards, the SDI data is photon noise limited, approaching the read-noise limit at separations  $> 2$ ”.

We converted our noise in electrons to attainable contrasts in magnitudes in the F1(1.625  $\mu\text{m}$ ) filter – contrast plots in  $\Delta\text{mag}$  are presented for all non-binary survey objects in Figs. 8 to 14 according to the H magnitude of the primary for the VLT and according to observing run for the MMT. For every observation which possesses an unsaturated acquisition image (typically  $10 \times 0.1$  s images taken over  $\sim 30$  s), the stellar peak in the unsaturated acquisition image was used to scale the saturated stellar peak in the saturated data images and thus attain accurate contrasts in magnitudes. For observations lacking an unsaturated acquisition image, contrast curves for other stars which had similar peaks, read noise values, and shape to the contrast curve in question were selected from the library of contrast plots in electron units. The peaks utilized for these matching contrast curves were then used to scale the observation missing an acquisition image. A peak of  $2.2 \times 10^5$  was adopted for  $\epsilon$  Eri (Kellner et al. 2007, Janson et al. 2007) and  $\epsilon$  Ind A (Geißler et al. 2007). We present contrast curves for 48 stars in this paper; the remaining six survey stars were either very close binaries, making it difficult to generate a contrast curve, or had particularly low quality datasets.

For the VLT data, attainable contrast depends on primary star H magnitude as well as seeing FWHM and Strehl ratio during the observation. For the brightest stars in the survey ( $H < 4.5$ ), we attain  $5\sigma$  contrasts of  $\Delta F1 \sim 12$  mag at separations of  $> 1$ ” from the star. For the faintest survey stars, we only attain  $5\sigma$  contrasts of  $\Delta F1 \sim 10$  mag  $> 1$ ” from the star. However, considerable spread in attained contrast is observed in each H magnitude

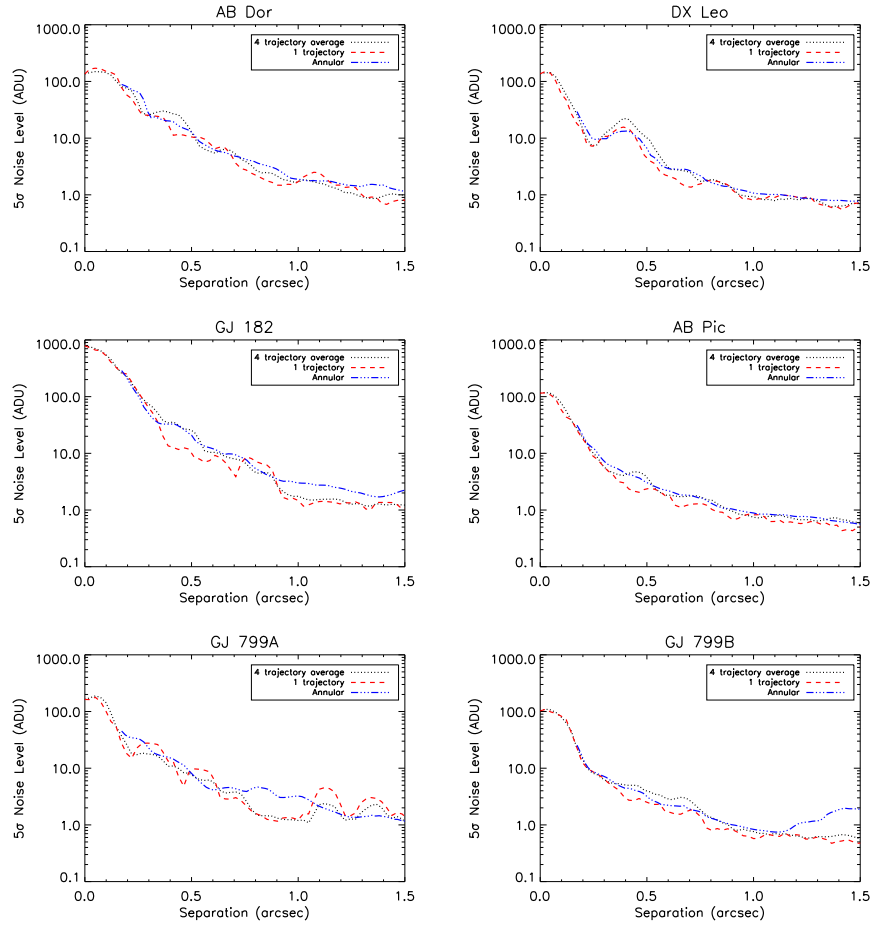


Fig. 6.— Comparison of Noise Curves generated in 3 different manners for a set of 6 typical program stars (upper left: AB Dor, upper right: DX Leo, middle left: GJ 182, middle right: AB Pic, lower left: GJ 799A, lower right: GJ 799B). Noise curves were generated by: 1) translating a  $6 \times 6$  pixel ( $0.1'' \times 0.1''$ ) box along a particular radial trajectory away from the center of the star image (typical PSF FWHM was 3-5 pixels) then calculating the standard deviation in the box at each point along this trajectory, 2) averaging noise curves generated along four such trajectories, and 3) calculating the standard deviation within annular regions 6 pixels in width centered on the primary PSF (spider diffraction spikes were not masked out in this case because they are already well removed by the spectral difference). In general, all three methods produce remarkably similar noise curves and are equally suitable for characterizing the noise properties of an observation. Since it preserves pixel to pixel contrast variations due to speckle noise, the single trajectory method better simulates the S/N issues encountered in searching for faint companions.

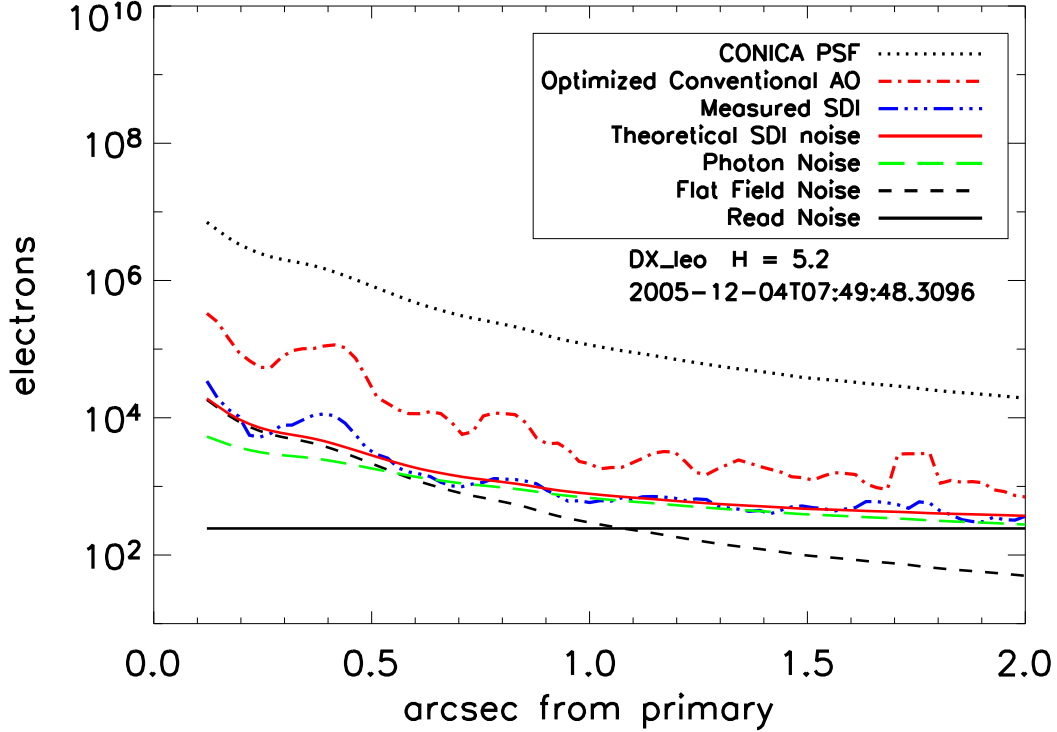


Fig. 7.— Sensitivity curve for DX Leo (18 pc, K0V, 115 Myr,  $V=7.05$ ,  $H=5.242$ ). This is 28 minutes of VLT SDI data. The CONICA PSF curve is the median combination of all the F1(1.575  $\mu\text{m}$ ) filter images for this dataset (with a gain correction applied which accounted for the number of exposures, dithers, and roll angles). The “optimized conventional AO” curve was generated by averaging images from all three filters at each roll angle, unsharp masking to remove low spatial frequencies, then subtracting the combinations at different roll angles from each other. The “measured SDI” data curve is the full reduced and differenced SDI data for this object (F1(1.575  $\mu\text{m}$ ) - F3a(1.625  $\mu\text{m}$ ) for two roll angles). The “theoretical SDI noise” curve is calculated from photon noise (long dashed green curve), flat-field noise (short dashed black curve), and read noise (solid black line) added in quadrature. Within 0.5”, the SDI data is “flat-field” noise limited. (In reality, we are limited by super speckle residuals within this radius. Our flat fields are accurate to the  $\sim 1\%$  level, but the speckle residuals  $< 0.5''$  vary more than this and thus dominate the SDI noise.) From 0.5” onwards, the SDI data is photon-noise limited, asymptotically approaching the read-noise limit at separations  $> 2''$ . For a complete set of sensitivity curves, see: <http://exoplanet.as.arizona.edu/~lclose/SDI.html>.

bin – most likely due to variations in observing conditions (seeing, Strehl ratio, etc.) across multiple observations. To quantify the effect of seeing on attainable contrast, in Fig. 15 we plot the seeing FWHM (averaged over the observation – the error bars on seeing are the seeing variations as measured by the standard deviation of the seeing over each observation) vs. attained  $5\sigma$  contrast at  $0.5''$  for 10 of the stars presented in Fig. 9 with H magnitudes between 4.5 – 5.5. For this sample of stars with similar H magnitudes, achievable contrast is roughly inversely proportional to the seeing FWHM. A fair amount of scatter is apparent in this plot and is due in part to seeing variations over the course of each observations. Seeing FWHM can vary considerably over the 20-40 minute timescale of a typical SDI observation, affecting the AO system performance and thus the achievable contrast.

However, higher attained contrast does not necessarily translate across the board to a lower minimum detectable planet mass. Although one might be able to attain a very high contrast ( $5\sigma$  contrast  $>11$  mag at  $1''$  limited by photon noise) for a bright young A star, one would have more luck searching for low luminosity planets around an intrinsically faint young M star ( $5\sigma$  contrast  $\sim 9$  mag at  $1''$  limited by read noise), since the inherent contrast difference expected between star and planet is considerably smaller. We obtained contrasts of  $\Delta H > 10$  mag ( $5\sigma$ ) at  $0.5''$  for 45% of target objects at the VLT and contrasts of  $\Delta H > 9$  mag ( $5\sigma$ ) at  $0.5''$  for 80% of our targets. This is more a statement on the spectral types in our sample than a performance related issue.

In general, the MMT SDI device performed at a slightly lower level than the VLT SDI device – attaining  $5\sigma$  contrasts 0.5-1 magnitude less than those achieved at the VLT for similar separation and primary star H magnitude. The lesser performance of the MMT system can be attributed to two factors. First, the diameter of the MMT is 6.5m versus the VLT which has an 8.2 m diameter – resulting in a considerable decrease in sensitivity. Additionally, the seeing sampled by the MMTAO system was not as stable as for the NACO AO system – Strehl ratios often changed dramatically over an observation, limiting the attainable contrast. However, the MMT SDI results still probe a higher contrast regime at separations  $<1''$  than is possible with standard AO techniques.

In order to determine what objects realistically can be detected for our survey stars, we must convert between our instrumental F1( $1.625\ \mu\text{m}$ ) filter magnitudes and H band magnitudes and then compare the H magnitudes to those expected from models of young planets (such as Burrows et al. 2003). To accomplish this, the spectra of both the primary and secondary components of each target must be taken into account. To convert from our F1 filter magnitudes into calibrated H band magnitudes we must calculate the H band magnitude offsets for both the primary star and a potential methane companion ( $\text{Offset}_A$  and  $\text{Offset}_B$  respectively):

$$\Delta H = H_A - H_B = (Offset_B + F1_B) - (Offset_A + F1_A) = (Offset_B - Offset_A) + \Delta F1 \quad (11)$$

For primary stars with spectral types F-K, we assume that the star has very little chromatic variation within the middle of the H band, so  $Offset_A$  is zero (see Fig. 1). For lower mass M stars, which are very red, the magnitude offset is not negligible. To take an extreme example, a very low mass M8 primary will have a magnitude offset of  $Offset_A = -0.12 \pm 0.08$  mag (calculated using the spectrum of the M8 star VB10, an H transmission curve, and our F1 filter transmission curve). The latest stars in our survey have spectral type M0- M5, so  $Offset_A$  will be  $< 0.1$  mag for these cases.

Any T3 or later companion to one of our survey stars will be blue compared to the primary and will appear “brighter” in the F1 filter than in the H band (in other words, it will have a higher “flux” in the F1 filter (# photons per unit bandwidth) – see Fig. 1) – so  $Offset_B$  will definitely be non-negligible. We calculated  $Offset_B$  for 18 objects with spectral types of T4.5-T8 (spectra from Knapp et al. 2004), then averaged together by spectral type to derive an average offset for each spectral type. For a T5 companion,  $Offset_{T5} = 0.5 \pm 0.05$  mag, for a T6 companion,  $Offset_{T6} = 0.6 \pm 0.07$  mag, and for a T8 companion,  $Offset_{T8} = 0.87 \pm 0.04$  mag. While we do not convert our full  $\Delta F1$  contrast plots to  $\Delta H$  contrast plots, for every survey star we calculate limiting  $\Delta H$  contrasts ( $5\sigma$  values), at 0.5” and 1.0”, equivalent separation in AU, apparent H magnitude, and absolute H magnitude for a T8 spectral type companion (since extrasolar planets are expected to have spectral type  $\gtrsim$  T8, Burrows et al. 2003). These results are presented in Tables 4 and 5. However, it is difficult to translate our absolute H magnitudes into model planet masses since we have assumed a T8 spectral type in our conversion between  $\Delta F1$  and  $\Delta H$  contrasts – but a companion which actually has the limiting absolute H magnitude we find (combined with the known age and distance of the system) may have a very different spectral type.

Since we cannot translate our H magnitudes directly into planetary mass companions, we followed the analysis of Masciadri et al. (2005) and translated theoretical planet models (Burrows et al. 2003, Baraffe et al. 2003) into H magnitudes then determined the minimum separation at which such a companion could be detected (at the  $5\sigma$  level) in our survey. The minimum separation at which a  $5 M_{Jup}$  or a  $10 M_{Jup}$  companion could be detected for each of our survey stars is shown in Table 6. Using the Burrows et al. (2003) models, for 50% of the cases in our survey we detect no  $5 M_{Jup}$  planets at separations larger than 18.6 AU and no  $10 M_{Jup}$  planets at separations larger than 7.5 AU. While these numbers are comparable to those found in Masciadri et al. (2005), our current survey actually attains higher contrasts on a case by case basis than Masciadri et al. (2005). Our median survey object has an age of 50 Myr whereas the median survey object of Masciadri et al. (2005)

has a considerably younger age of 12 Myr – the star-planet contrast is less at younger ages, thus one would expect a younger object to have a lower minimum separation at a given attained contrast than a similar but older object. For the 10 objects in common between the surveys, our survey attains lower minimum separations for 8 out of 10 objects (we note also that the two objects for which we did not attain lower separations were particularly low quality SDI datasets). Minimum detectable separations for a  $5 M_{Jup}$  object for the 10 objects in common are plotted in Fig. 16 (using the ages adopted by Masciadri et al. 2005). Our survey is generally more sensitive than Masciadri et al. (2005) on shared stars because the SDI technique allows us to achieve higher contrasts closer to the star (separations of  $0.3''$  -  $1.0''$ ) compared to the deep broad-band imaging technique of Masciadri et al. (2005), thus allowing us to potentially detect companions at tighter separations. We also shared 4 survey objects in common with Lowrance et al. (2005) and 1 object ( $\epsilon$  Eri) in common with Luhman and Jayawardhana (2002). In all of these cases, our limiting contrasts at  $0.5''$  ( $\Delta H \sim 10$ -11 mag) are considerably higher than those attained in these previous surveys ( $\Delta H \sim 6.5$ -7.6 mag), thus we are sensitive to planets at much smaller separations with SDI.

### 3.4. Survey Completeness

One would not expect a planet to be detectable at all phases of its orbit – to really understand the types of planets to which we are sensitive, we must take orbital motion into account and translate separations on the sky into orbital semi-major axes ( $a$ ). To this end, we generated contour plots of fractional completeness as a function of mass and semi-major axis. For every survey star, we simulate 10000 planets for each combination of mass and semi-major axis. Eccentricities are drawn from a distribution of eccentricities consistent with known radial velocity planets. Standard distributions were used to randomly compute viewing angle and orbital phase, giving an instantaneous separation between star and planet. We use the distance, age, spectral type, and H-band magnitude of the star, and luminosity as a function of mass, calculated from the Burrows et al. (2003) models, to provide each simulated planet a separation on the sky in arcseconds, and an H-band flux ratio compared to its parent star. Combining this with the SDI contrast curve for each star in the survey, we can then determine the percentage of simulated planets detected as a function of mass and semi-major axis for each survey star. Contour plots for a set of 4 typical program stars (AB Dor, DX Leo, GJ 182, and GJ 799B) are presented in Fig. 17. Note that we conservatively assume only T-type objects can be detected, hence masses  $> 10 M_{Jup}$  are not considered for many young targets. The value attached to each contour level defines the completeness of our observation to detecting (at the  $5\sigma$  confidence level) a planet with the given semi-major axis and mass. It is worth noting that the only assumptions necessary for the generation of

these plots is the eccentricity distribution of planets and the Burrows et al. 2003 models.

We use this method to summarize our survey completeness in Fig. 18. Having computed the completeness for each star to planets at various masses and semi-major axes, we take slices at representative values of the semi-major axis, and present the number of stars in our 54 star survey which are at least 50% complete to such a planet. Our survey places the strongest constraints on planets between 6-10  $M_{Jup}$  with semi-major axes between 20-40 AU. With 20 such stars (with 50% or greater completeness in this mass/semi-major axis range) surveyed without a detection of a planet, a simple way of interpreting our results (though without statistical rigor) is that we would expect the frequency of such planets to be of order 10% or less.

The evolutionary models of Burrows et al. (2003) utilize a “hot start” initial condition which, while appropriate for brown dwarfs, is possibly significantly different from the actual initial origins of planets. The Burrows et al. (2003) models begin with a high-temperature, high-entropy hydrogen-helium sphere which is allowed to radiate and cool over time. In contrast, a planet forms when gas accretes onto a rocky core, according to the core-accretion models of Ida and Lin (2005) and the disk instability models of Boss (2003). Recently, Marley et al. (2006) simulated model planets with more realistic (lower entropy) initial conditions. These model planets have significantly lower luminosities at young ages ( $<1$  Gyr). Model planets also converge to the “hot start” evolutionary tracks at different times according to mass – a 1  $M_{Jup}$  model converges to traditional tracks by 20 Myr, while a 10  $M_{Jup}$  requires up to 1 Gyr to match traditional tracks. Currently, H band magnitudes for these models are not yet available, but will be available in Spring 2007 (private communication, J. Fortney). When H band magnitudes are available, we will repeat this analysis using these new models.

### 3.5. Sensitivity Case Study: AB Dor with Simulated Planets

Since our survey data are highly saturated in the core of the image, it is difficult to place simulated objects in our data with a high degree of positional accuracy, as there is no external reference for position between data taken at different dithers and roll angles. However, as part of the SDI survey observations, our team discovered a close-in (0.156”) companion (hereafter AB Dor C) to the young star AB Dor (Close et al. 2005b). While this companion is a very low mass M star ( $0.090 \pm 0.005 M_{Sun}$ ,  $M5.5 \pm 1$ , Close et al. 2005b, 2007b) and hence, does not possess methane absorption features, it is still clearly detected in our SDI data. In our second AB Dor dataset where AB Dor C is separated from its primary by 0.2” (Nielsen et al. 2005), the AB Dor C source can be used to our advantage

as a reference position from which to offset – allowing us to add simulated planets into this dataset with highly accurate positions and relative fluxes independent of our “pipeline” calculated centroids.

Simulated planets were produced by scaling  $\sim 10 \times 0.1$  s unsaturated images of AB Dor A taken right before the example dataset. Planets were simulated with  $\Delta F1(1.575\mu\text{m}) = 9, 10, 11,$  and  $12$  mag and with methane break strengths appropriate for T5, T6, and T8 spectral types. Methane break strengths were calculated using the methane spectral index defined in Section 3.2. Photon noise and zero points appropriate for each object was added using the IRAF `artdata/mkobject` tool. The photometric zero point was calculated from AB Dor C.

A fully reduced 28 minute dataset of AB Dor A (70 Myr K1V at a distance of 14.98 pc,  $V=6.88$ ) from the VLT SDI device is presented in Fig. 19 with simulated planets added at separations of  $0.4''$ ,  $0.6''$ ,  $0.8''$ ,  $1.0''$ ,  $1.2''$ ,  $1.4''$ ,  $1.6''$ ,  $1.8''$ ,  $2.0''$ , and  $2.2''$  from the primary ( $\Delta F1(1.575\mu\text{m}) = 9, 10, 11,$  and  $12$  mag and spectral type T8). Past  $0.7''$ , the  $\Delta F1(1.575\mu\text{m}) = 10$  simulated planets are detected with  $S/N > 10$ . The  $2.2''$  object falls off the edge of the aperture in several dithers and thus appears somewhat attenuated compared to the other simulated objects. Maximum achievable companion contrast at the  $5\sigma$  level as a function of distance from the star is plotted in Fig. 20. The residual noise curve for this star (see section 3.3) is also overplotted. Contrast curves ( $5\sigma$ ) calculated with both techniques agree well with each other. Using the magnitude offsets developed in section 3.4, we convert our  $\Delta F1(1.575\mu\text{m})$  contrasts into  $\Delta H$  for each spectral type. We adopt  $\text{Offset}_A = 0$  mag,  $\text{Offset}_B = 0.5$  mag for a T5 object,  $\text{Offset}_B = 0.6$  mag for a T6 object, and  $\text{Offset}_B = 0.87$  mag for a T8 object.  $\Delta H$  vs. separation in arcsec is presented in Fig. 21.

$\Delta F1$  contrasts were translated into planet masses using the 100 Myr models of Burrows et al. (2003). According to the 100 Myr old model, objects with mass  $\leq 10 M_{Jup}$  will have  $T_{eff} < 900$  K – these objects are reliably of spectral types later than T7 (temperature scale from Burgasser et al. 2006). Thus, we adopt the T8 spectral type curve for this analysis. AB Dor has a likely age of 50-70 Myr (Nielsen et al. 2005, Close et al. 2007b) – we interpolate the models of Burrows et al. (2003) to derive masses at these ages as well. The minimum detectable planet mass as a function of distance from the star is plotted in Fig. 22. Adopting an age of 70 Myr for AB Dor A, we can detect a  $5 M_{Jup}$  planet 12 AU from the star. However, as noted above, the Burrows et al. 2003 models utilize a hot start initial condition which may be inappropriate for a young planet. The Marley et al. (2006) models utilize more appropriate initial conditions and when H band magnitudes become available for these models, we will repeat this analysis.



### 3.6. Comparison with Other Direct Detection Methods

We believe that our SDI images are the highest contrast astronomical images ever made from ground or space for methane rich companions  $\leq 1''$  from their star. To substantiate this claim, we compare our SDI contrast curves with those produced using a variety of other competing methods (Azimuthal Differential Imaging (ADI), Marois et al. 2006, Lyot Coronagraph, Hinkley et al. 2007, HST NICMOS, Schneider et al. 2003, K-band Keck AO, Schneider et al. 2003, and NACO deep imaging in the Ks band, Masciadri et al. 2005). Comparison contrast curves are presented in Fig. 23. Apart from the Lyot and NICMOS curves, all curves are from  $\geq 8\text{m}$  class telescopes. For ease of comparison, we convert our  $\Delta F1=1.575 \mu\text{m}$  SDI contrast curve into the equivalent  $\Delta H$  contrast appropriate for a T8 spectral type companion. For methane rich companions, SDI provides improved contrast by 1-4 mag within  $1''$  as compared to other methods.

### 3.7. New and Confirmed Close Binary Stars

A number of close binary stars were discovered or confirmed during our survey. In Table 7, we present separations and position angles measured from unsaturated SDI images of these stars acquired before each full SDI dataset was taken. These values are meant as estimates, hence, no error estimate is provided. We discovered close stellar companions to HIP 9141 ( $0.15''$  measured SDI separation), AB Dor A ( $0.16''$  measured SDI separation, see Close et al. 2005a), HD 48189A ( $0.14''$  measured SDI separation), HD 135363 ( $0.26''$  measured SDI separation) and CD-64 1208 ( $0.18''$  measured SDI separation). The  $<0.5''$  separation between the primary stars and these object makes it highly improbable that they are background objects. Additionally, we confirmed the close binary RXJ 1243.6-7834 ( $0.068''$  measured SDI separation) discovered by Brandner et al. (2000), the visual double LH 98 062 ( $2.4''$  measured SDI separation) discovered by Mochnicki et al. (2002), the spectroscopic binary TWA 4 ( $0.78''$  measured SDI separation) discovered by Torres et al. (1995) and the close binary EK Dra ( $0.67''$  measured SDI separation) discovered by Metchev and Hillenbrand (2004).

### 3.8. Candidate Identification / Elimination

Survey data were examined for planet candidates by eye and also using automated detection algorithms; generally, the human eye proved more effective for detecting candidates. We identified 8 very tentative planet candidates at the VLT which passed the following tests:

- 1) Candidate must appear at the appropriate positions in the full reduced data. (i.e. candidate image position must jump by the appropriate roll angle.)
- 2) Candidate must appear (at least marginally) at the appropriate position in each of the separate roll angle images
- 3) Candidates detected in the F1(1.575  $\mu\text{m}$ ) - F3a(1.625  $\mu\text{m}$ ) difference should also be detected in the F2(1.6  $\mu\text{m}$ ) - F3a(1.625  $\mu\text{m}$ ) difference as well.

These extremely tentative ( $<2\sigma$ ) candidates are noted in the comments column of Table 1, with the predicted mass (from the models of Burrows et al. 2003) and separation had it been real. No candidates were detected with  $>3\sigma$ . None of the 8 tentative candidates were detected at a second epoch, thus the survey reached a null result for extrasolar planets at the  $\sim 3\sigma$  level and certainly at the  $5\sigma$  level analyzed here.

### 3.9. Planet Detectability

To determine what sort of planets we can detect in this survey, we converted our contrast curves in  $\Delta\text{mag}$  units into minimum detectable mass vs. separation (assuming a late T to early Y spectral type for all possible objects and using the models of Burrows et al. (2003)). We calculated minimum detectable mass vs. separation for all stars with contrast curves in Figs. 8 to Figs. 14; minimum detectable mass vs. separation is presented for a set of four typical survey stars (AB Dor, DX Leo, GJ 182, and GJ 799B) in Fig. 24. However, to detect an object of any given mass requires that such an object exists around its parent object! The likelihood of detecting any object at a given radius is a combination of the minimum detectable mass for the parent star at that radius and the likelihood of such an object existing. Therefore it is very important to fully characterize and understand the expected distribution of objects around each survey star. The results of the survey then also constrain the possible distribution of extrasolar planets as a function of radius.

To this end, we ran detailed Monte Carlo simulations to characterize the ensemble of planets expected to exist around each star. We conduct a similar simulation to that used to produce the contour plots of Fig. 17, as described in Section 3.4 (these simulations are described in much more depth in Nielsen et al. 2006). In contrast to the production of the contour plots, we simulate  $10^6$  planets instead of  $10^4$ , and mass and semi-major axis are now assigned distributions of their own. The mass and semi-major axis distributions, like the distribution for eccentricity, are produced by considering the population of published radial velocity planets (e.g. Butler et al. 2006), with mass and eccentricity both chosen to fit the histograms from observed planets. Semi-major axis has been observed to follow a

distribution of  $N(a) \propto a^{-1}$  for radial velocity planets (Wright et al. 2005). Since the radial velocity method has an inherent bias toward close-in planets (which have shorter orbital periods and larger radial velocity amplitudes), we attempt to correct for this by assuming a power-law distribution that is constant in semi-major axis – i.e.  $N(a) \propto \text{constant}$ . We consider the results of Fischer and Valenti’s (2005) volume-limited sample, and choose an outer limit for the semi-major axis distribution such that, for stars in the metallicity range in our sample, each star is expected to host one planet. This is done by integrating the semi-major axis distribution from 0.02 AU (corresponding to HD 41004Bb, the closest-in exoplanet known thus far) to 2.5 AU, the detection limit for the sample of Fischer and Valenti (2005), then noting the fraction of stars with planets in the metallicity range ( $-0.5 < [\text{Fe}/\text{H}] < 0.25$ ) of our target stars (4.1%) and choosing an upper cut-off to the distribution when the integral reaches 100%. This gives us a constant probability distribution for semi-major axis between 0.02 and 45 AU that contains the same number of planets found in the  $<2.5$  AU radial velocity survey.

The ensemble of simulated planets is shown for our set of four typical stars in Fig. 24. Simulated planets which are detected are plotted as blue dots and those that remain undetected are plotted as red dots. In addition to the contrast plot, we also consider a planet “undetectable” when its apparent H magnitude drops below 21 mag (a limit set by our total integration time), or when the planet’s temperature rises above 1400 K (given as a function of age and planet mass by Burrows et al. 2003). Above this temperature, the strength of the  $1.62 \mu\text{m}$  methane break weakens to the point that the SDI method loses effectiveness. Since we assume that each program star possesses exactly one planet that follows the distributions given above, we can assign a detection probability for that star from the percentage of the simulated planets that are detectable at the  $5\sigma$  level. For our 48 program stars (consisting of 40 stars with ages  $>250$  Myr and closer than 50 pc, 1 10 Myr old star at a distance of 67 pc, 3 stars with known RV planets and 4 nearby solar analogues) which possess contrast curves, the average detection probability is 8.0%, the median detection probability is 4.1%, and the maximum detection probability is 47%. We have chosen to leave the older stars in this sample in our statistics even though their detection probabilities are essentially zero. Integrating over the probability distribution of our program stars, in Fig. 25 we plot the number of planets we expect to detect as a function of total stars observed, ordering the results so that the best stars (highest detection probabilities) are considered first. For the 48 stars in our surveys for which we acquired contrast curves, we expect to detect a total of 3-4 planets (3.8 to be exact) based on the above assumptions. Thus, our survey null detection rules out this exoplanet distribution at the 98% ( $2.0\sigma$ ) level. It is important to note that this null result shows that this particular combination of assumptions (mass distribution, eccentricity distribution, constant semi-major axis distribution, upper limit to semi-major

axis at 45 AU, assumption that each star has a planet, and the mass-luminosity conversion from the models of Burrows et al. 2003) is ruled out to this confidence level; determining which individual assumptions are incorrect will require data beyond that of the current survey. These simulations (including a variety of other possible exoplanet distributions) are discussed in more detail in Nielsen et al. (in prep.) Nevertheless, our null detection in this survey sets strong upper limits on the distribution of young massive extrasolar planets  $>5$  AU from their primaries and provides valuable constraints for theories of planet formation and migration.

#### 4. Conclusions

We obtained datasets for 54 stars (45 stars were observed in the southern sky at the VLT, 11 stars were observed in the northern sky at the MMT, and 2 stars were observed at both telescopes). In our VLT data, we achieved H band contrasts  $> 10$  mag ( $5\sigma$ ) at a separation of  $1.0''$  from the primary star on 45% of our targets and H band contrasts of  $> 9$  mag at a separation of  $0.5''$  on 80% of our targets. With this degree of attenuation, we should be able to image ( $5\sigma$  detection) a  $5 M_{Jup}$  planet 15 AU from the star around a 70 Myr K1 star at 15 pc or a  $5 M_{Jup}$  planet at 2 AU from a 12 Myr M star at 10 pc. We believe that our SDI images are the highest contrast astronomical images ever made from ground or space for methane rich companions within  $1''$  of their primary star.

Eight tentative candidates were identified (none with  $S/N > 2\sigma$ ). Had these candidates been real, they would have possessed separations of 3 - 15.5 AU and masses of 2-10  $M_{Jup}$ . However, none of the candidates were detected in second epoch observations. Thus, we find a null result from our survey. Nonetheless, our result still has serious implications for the distribution of extrasolar planets. In the course of our survey, we also discovered 5 new close stellar binary systems with measured separations of  $0.14''$  to  $0.26''$ .

For 20 of our survey stars, we attained 50% completeness for 6-10  $M_{Jup}$  planets at semi-major axes of 20-40 AU. Thus, our completeness levels are sufficient to significantly test theoretical planet distributions. From our survey null result, we can rule out (at the 98%/ $2.0\sigma$  level) a model planet population using a constant distribution ( $N(a) \propto \text{constant}$ ) of planet semi-major axis out to a distance of 45 AU (a number of further exoplanet distribution models are considered in Nielsen et al. in prep.). Our null detection in this survey sets strong upper limits on the distribution of young massive extrasolar planets  $>5$  AU from their primaries and provides valuable constraints for theories of planet formation and migration.

This publication is based on observations made with the MMT and the ESO VLT at

Paranal Observatory under programme ID's 074.C-0548, 074.C-0549, and 076.C-0094. This publication makes use of data products from the Two Micron All Sky Survey, which is a joint project of the University of Massachusetts and the Infrared Processing and Analysis Center/California Institute of Technology, funded by the National Aeronautics and Space Administration and the National Science Foundation. We thank René Racine for refereeing this paper and for useful suggestions and Remi Soummer for suggesting the method of contour plots to present our detection limits. BAB is supported by the NASA GSRP grant NNG04GN95H and NASA Origins grant NNG05GL71G. LMC is supported by an NSF CAREER award and the NASA Origins of the Solar System program. ELN is supported by a Michelson Fellowship.

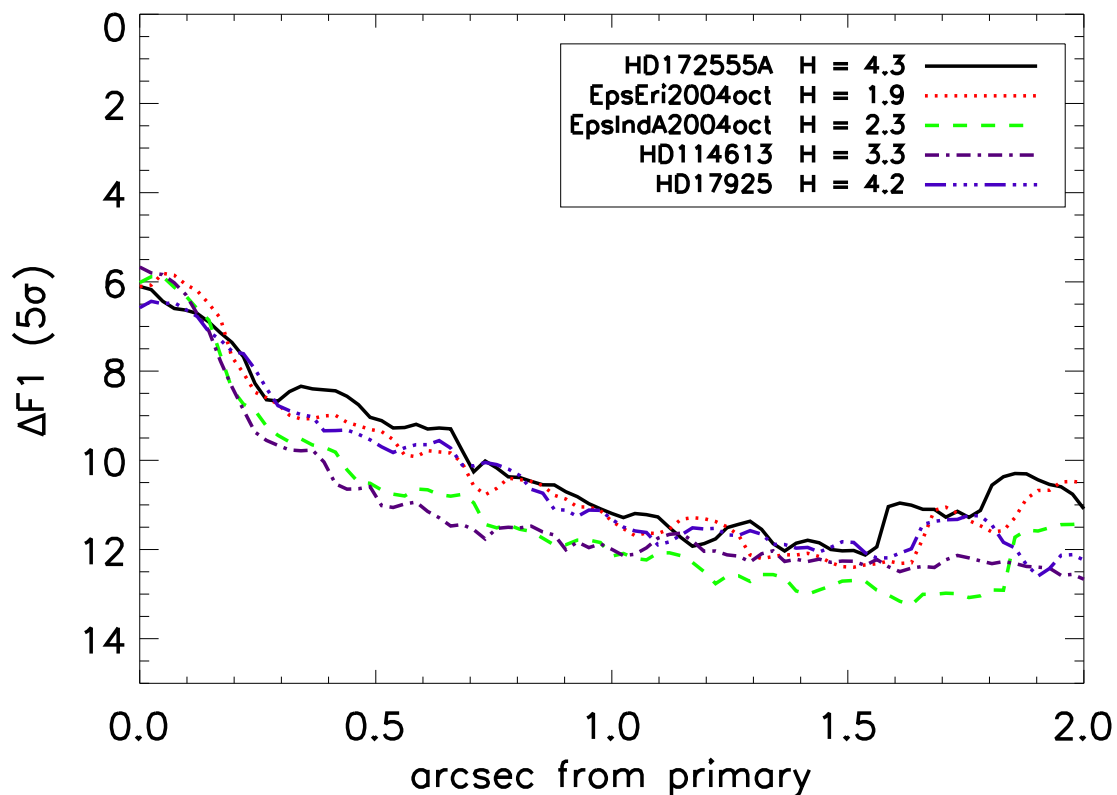


Fig. 8.—  $5\sigma$  Contrasts for VLT SDI survey objects with  $H < 4.5$  in the F1(1.575  $\mu\text{m}$ ) filter. These contrast curves were generated by translating a  $6\times 6$  pixel ( $0.1''\times 0.1''$ ) box along a particular radial trajectory away from the center of the star and then calculating the standard deviation within that box as a function of radius. Curves were generated from the full reduced and differenced SDI data for each object (F1(1.575  $\mu\text{m}$ ) - F3a(1.625  $\mu\text{m}$ ) for two roll angles).

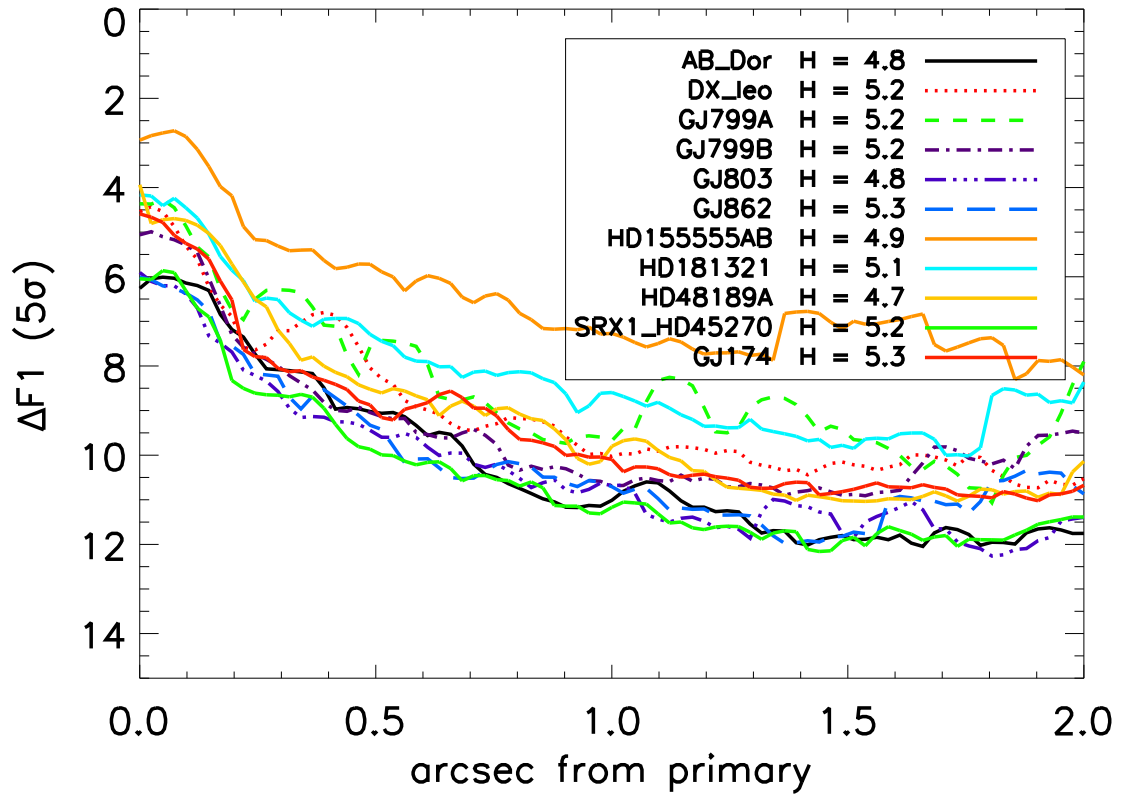


Fig. 9.— Same as Fig. 8 but for VLT SDI survey objects with  $5.5 > H > 4.5$ .

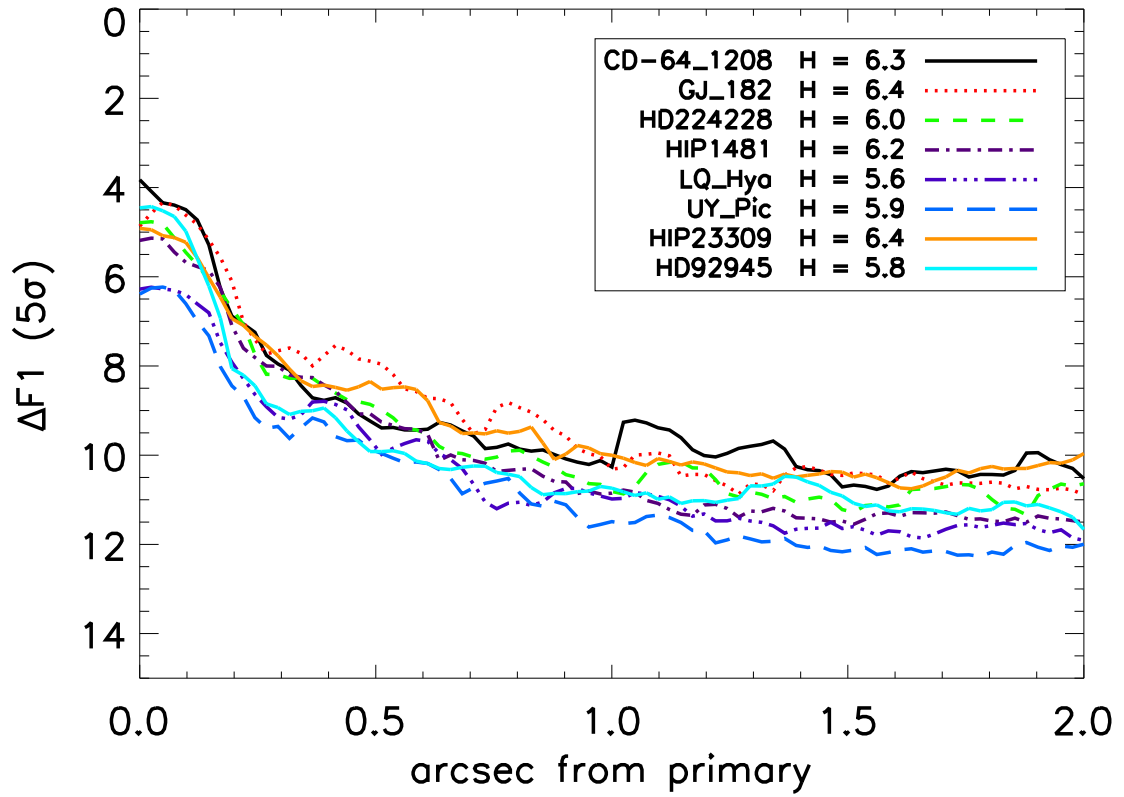


Fig. 10.— Same as Fig. 8 but for VLT SDI survey objects with  $6.5 > H > 5.5$ .



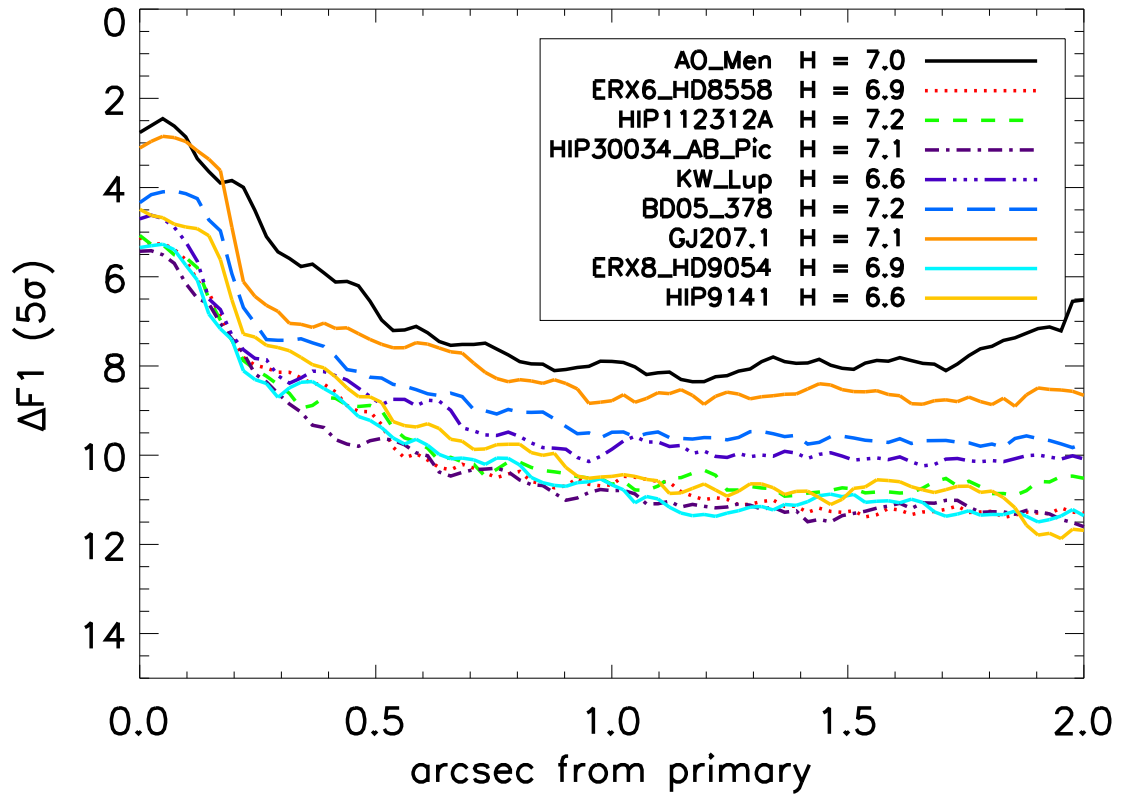


Fig. 11.— Same as Fig. 8 but for VLT SDI survey objects with  $7.5 > H > 6.5$ .

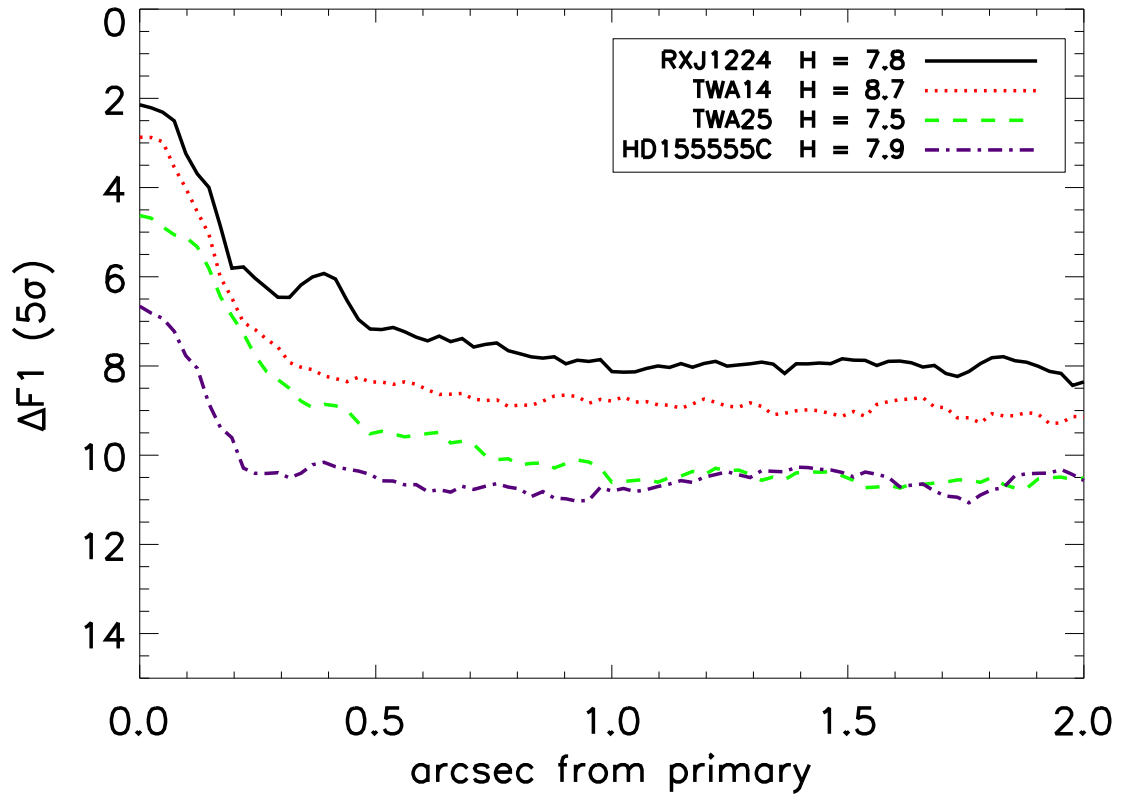


Fig. 12.— Same as Fig. 8 but for VLT SDI survey objects with  $H > 7.5$ .

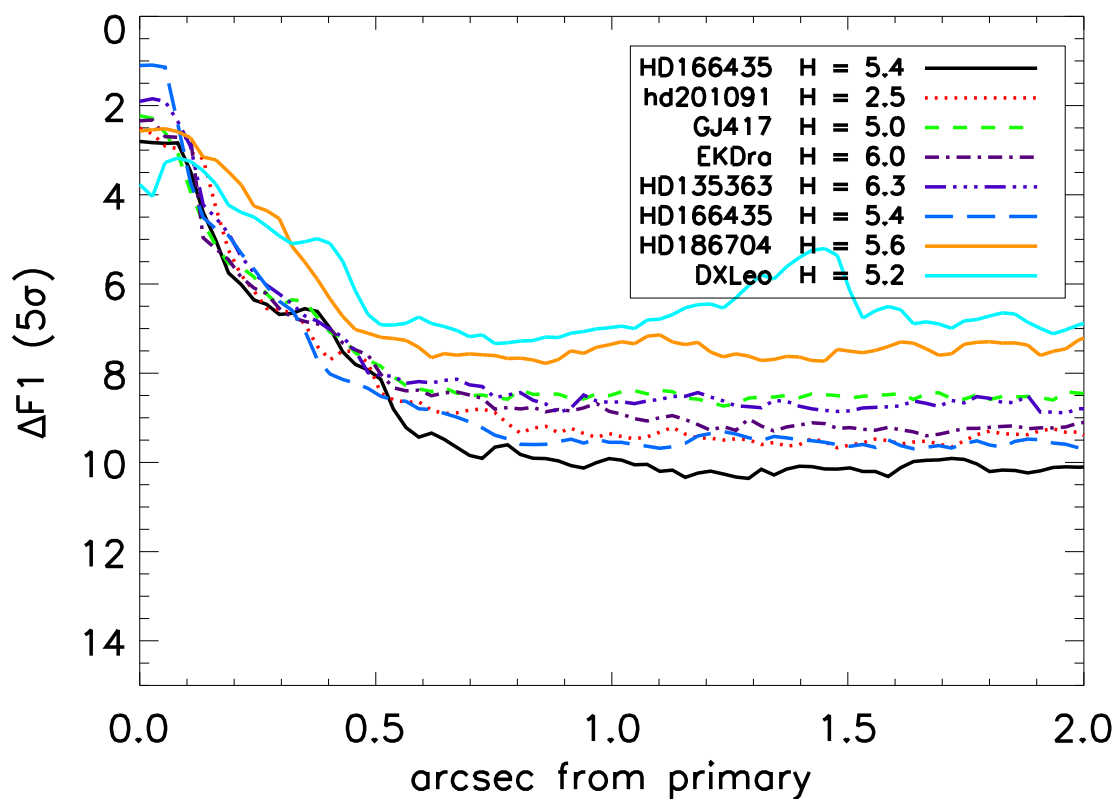


Fig. 13.—  $5\sigma$  contrasts for MMT SDI survey objects observed in May 2005. These contrast curves were generated by translating a  $6\times 6$  ( $0.1''\times 0.1''$ ) pixel box along a particular radial trajectory away from the center of the star and then calculating the standard deviation within that box as a function of radius. Curves were generated from the full reduced and differenced SDI data for each object (F1( $1.575\ \mu\text{m}$ ) - F3a( $1.625\ \mu\text{m}$ )) for two roll angles.

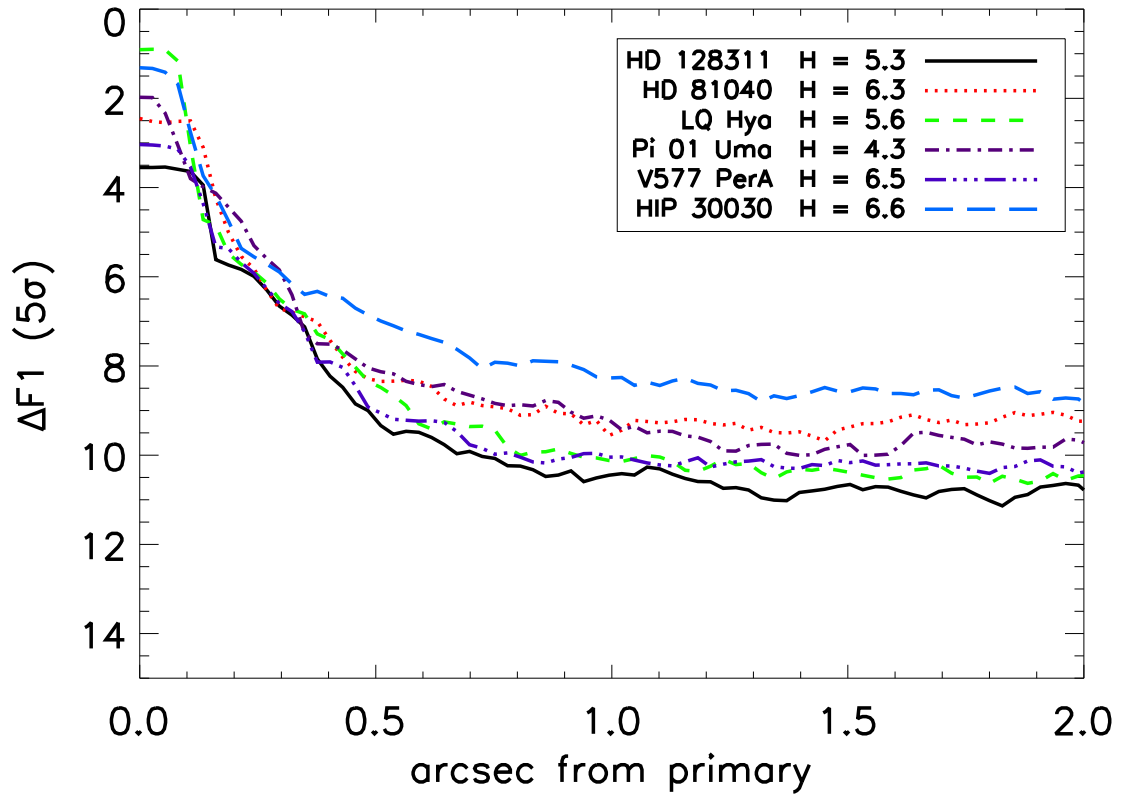


Fig. 14.— Same as Fig. 13 but for MMT SDI survey objects observed in February 2006.

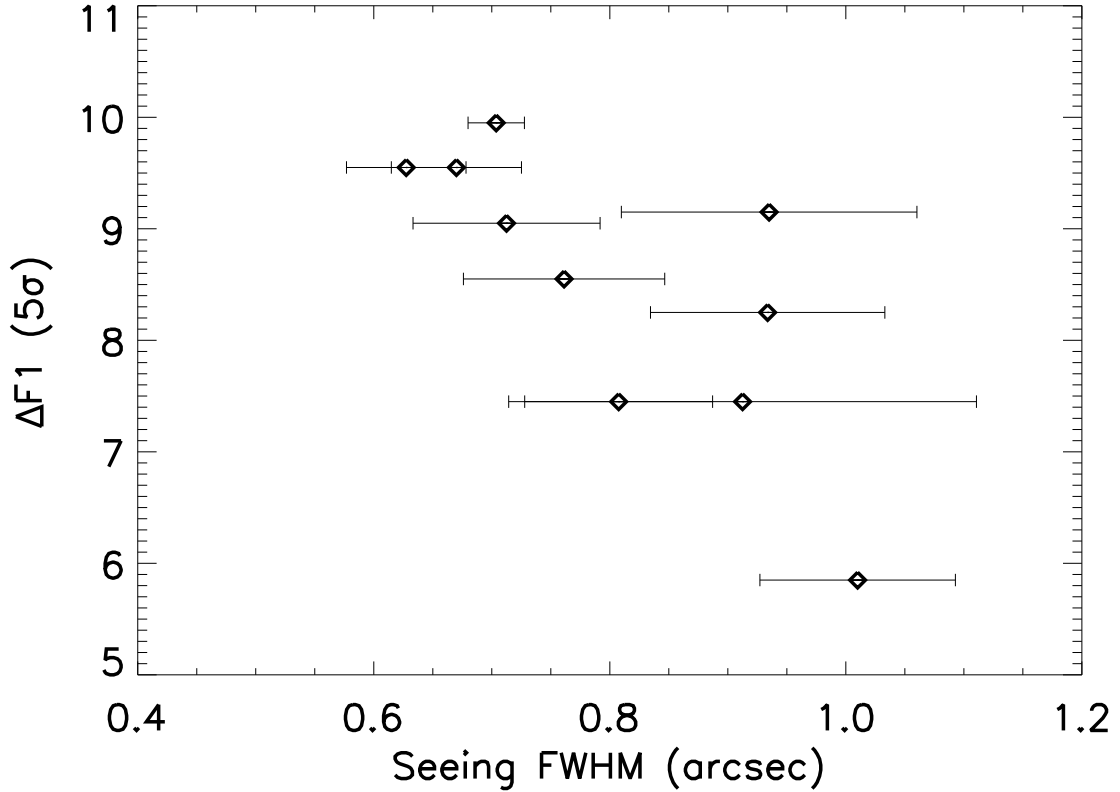


Fig. 15.— Seeing FWHM (averaged over each observation) vs. attained  $5\sigma$  contrast at  $0.5''$  separation from the primary star for 10 of the stars presented in Fig. 9 with H magnitudes between 4.5 – 5.5. The error bars on seeing are the seeing variation (as measured by the standard deviation of the seeing) over each observation. For this sample of stars with roughly the same H magnitude, achievable contrast varies roughly inversely with the average seeing FWHM. Scatter in this plot is in part due to the fact that seeing FWHM can change considerably over a 20-40 minute long observation.

## 5 $M_{Jup}$ Planet Detection Limit

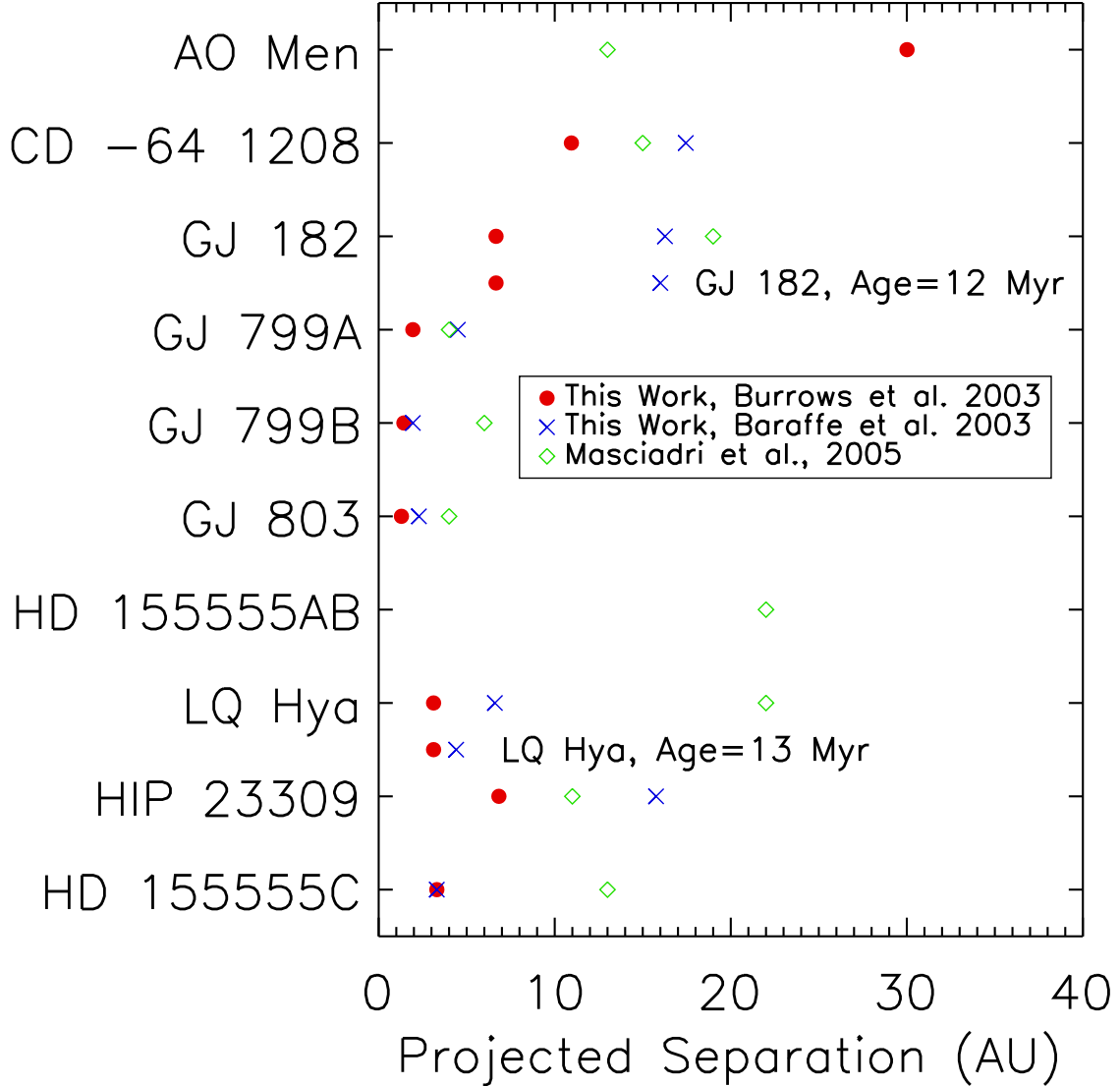


Fig. 16.— Minimum detectable planet separations for a  $5 M_{Jup}$  planet for the 10 objects in common between this survey and Masciadri et al. (2005) who used VLT NACO without SDI. For the purpose of comparison, we have adopted ages from Masciadri et al. (2005); we note our preferred age on the figure where our adopted ages differ from Masciadri et al. (2005). We translated theoretical  $5 M_{Jup}$  planet models (Burrows et al. 2003, Baraffe et al. 2003) into H magnitudes for these 10 cases then determined the minimum separation at which such a companion could be detected (at the  $5\sigma$  level) in our survey. For the 10 objects in common between the surveys, our SDI survey attains lower minimum separations for 8 out of 10 objects (we note also that the two objects for which we did not attain lower separations were particularly low quality AO/SDI datasets).

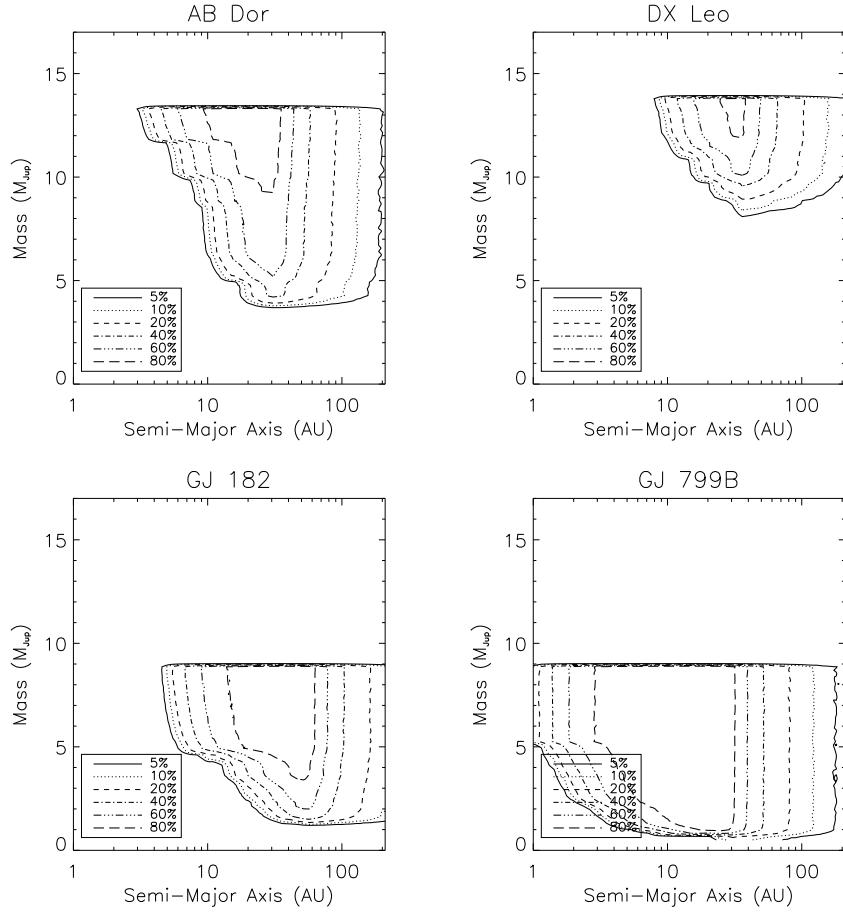


Fig. 17.— Planet detection completeness contour plots for a set of 4 typical program stars (upper left: AB Dor, upper right: DX Leo, lower left: GJ 182, lower right: GJ 799B). For a given mass and semi-major axis, 10,000 planets are simulated by our Monte Carlo method, over the expected distributions of eccentricity, orbital phase, and viewing angle. Given the parameters of the target star and the models of Burrows et al. (2003), we determine what fraction of the simulated planets are detectable at the  $5\sigma$  level given the contrast plot for that star. The contours show this detection probability across the 100,000 different combinations of mass and semi-major axis considered in this plot. The strong upper limit in mass is set by our conservative  $<1400$  K limit for the methane break required for a robust SDI detection. In these models, we simply do not allow an object with  $T_{\text{eff}} > 1400$  K to be detected, when in reality SDI can detect such non-methane objects (e.g. AB Dor C, Close et al. 2005b, Nielsen et al. 2005). For a complete set of planet detection completeness contour plots, see: <http://exoplanet.as.arizona.edu/~lclose/SDI.html>.

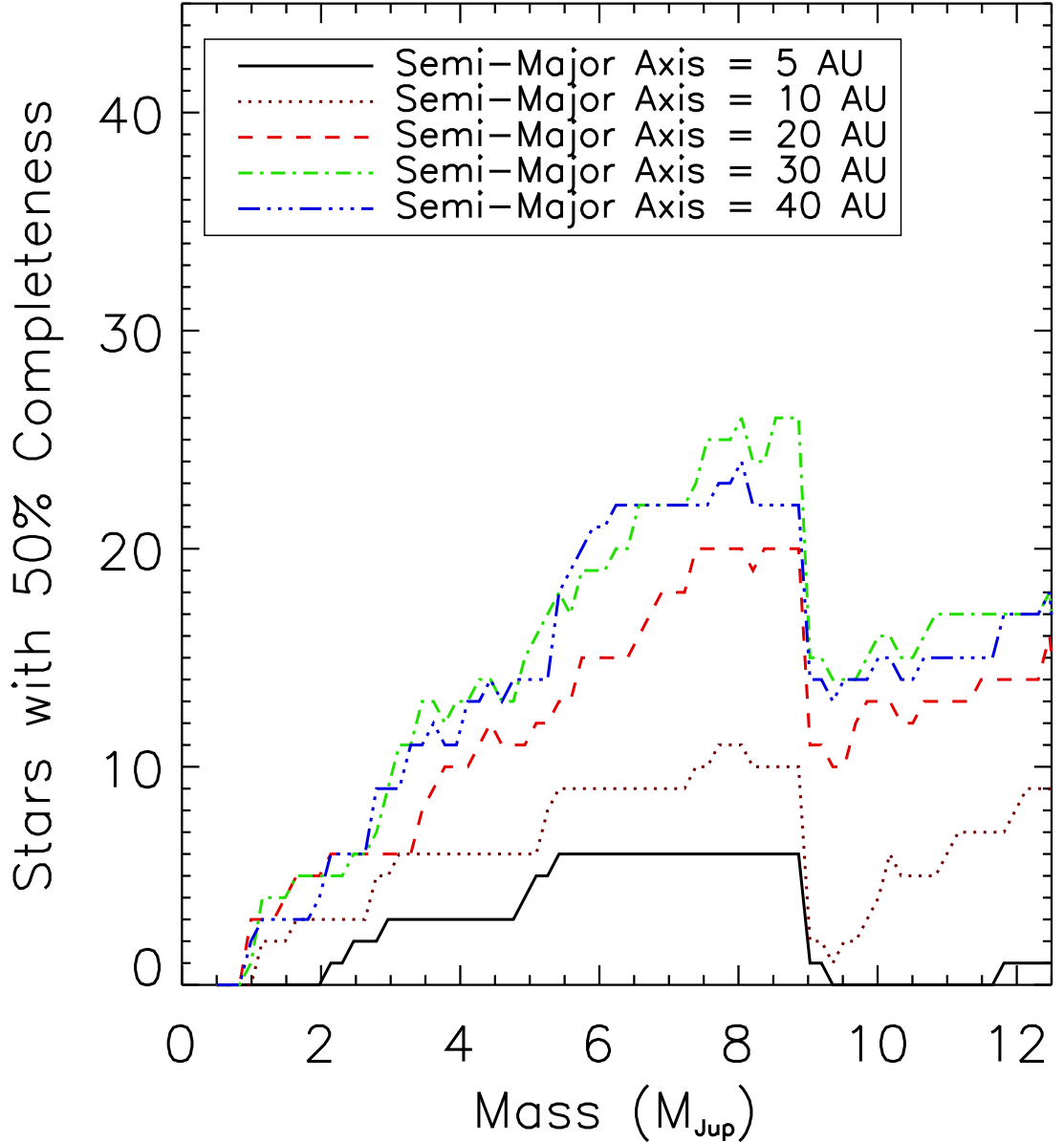


Fig. 18.— Our 50% completeness levels. Combining the results of Fig. 17, we consider individual values of the semi-major axis across the planetary mass range, and at each combination calculate the total number of stars in our survey (out of a total of 54) where the fraction of such planets, given by the Monte Carlo Simulation, that can be detected at the  $5\sigma$  level is 50% or greater. *Clearly, our survey is best able to place constraints on planets between 6 and 10  $M_{Jup}$ , and with semi-major axis between 20 and 40 AU.* The decrease in sensitivity for masses  $>7 M_{Jup}$  is due to the fact that such high mass planets are too hot to possess significant methane absorption if they are very young and, thus, are not ideal SDI targets. The higher completeness for 7-8  $M_{Jup}$  planets for semi-major axis of 30 AU vs. semi-major axis of 40 AU is due to the small field of view of the SDI device; planets with semi-major axes  $> 30$  AU can fall outside the SDI field in some of these cases.



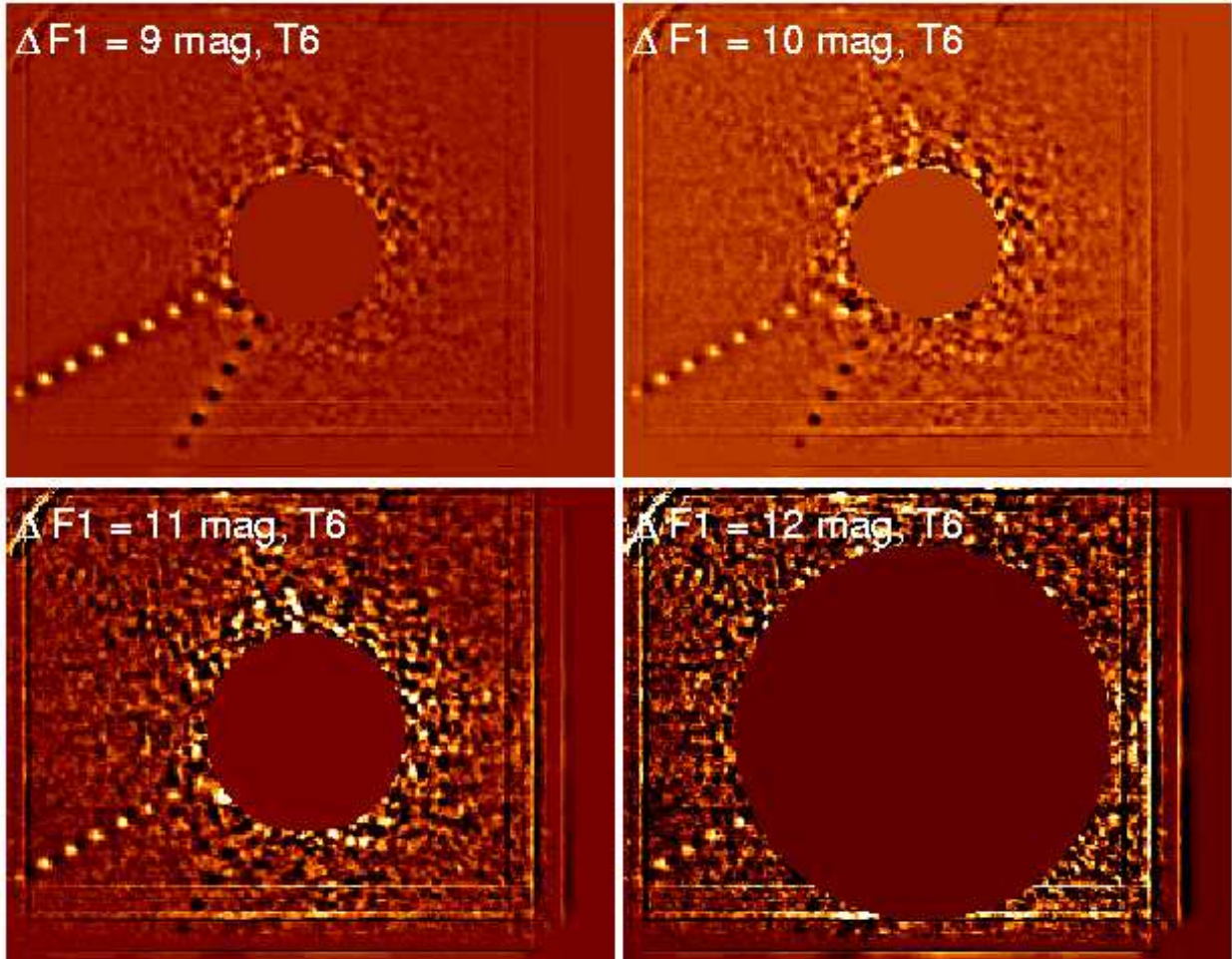


Fig. 19.— A complete reduced dataset of AB Dor A (28 minutes of data at a series of rotator angles  $-0^\circ, 33^\circ, 33^\circ, 0^\circ$ ) from the VLT SDI device. Simulated planets have been added every  $0.2''$  from the star ( $0.4'', 0.6'', 0.8'', 1.0'', 1.2'', 1.4'', 1.6'', 1.8'', 2.0'',$  and  $2.2''$ ) with  $\Delta F1(1.575\mu\text{m}) = 9 \text{ mag}$  (upper left, (attenuation in magnitudes in the  $1.575 \mu\text{m}$  F1 filter),  $10 \text{ mag}$  (upper right),  $11 \text{ mag}$  (lower left) and  $12 \text{ mag}$  (lower right) fainter than the star. The  $0.4''$  object falls within the inner dark circle (dark circle radius of  $0.5'', 0.5'', 0.7'',$  and  $1.3''$  respectively for the 9, 10, 11, and 12 mag objects); the  $2.2''$  object falls outside the frame aperture in a number of dither images and thus is detected with lower S/N than the other objects. These simulated planets are scaled from unsaturated images of AB Dor A taken right before the example dataset (and have fluxes and photon-noise in each filter appropriate for a T6 object).

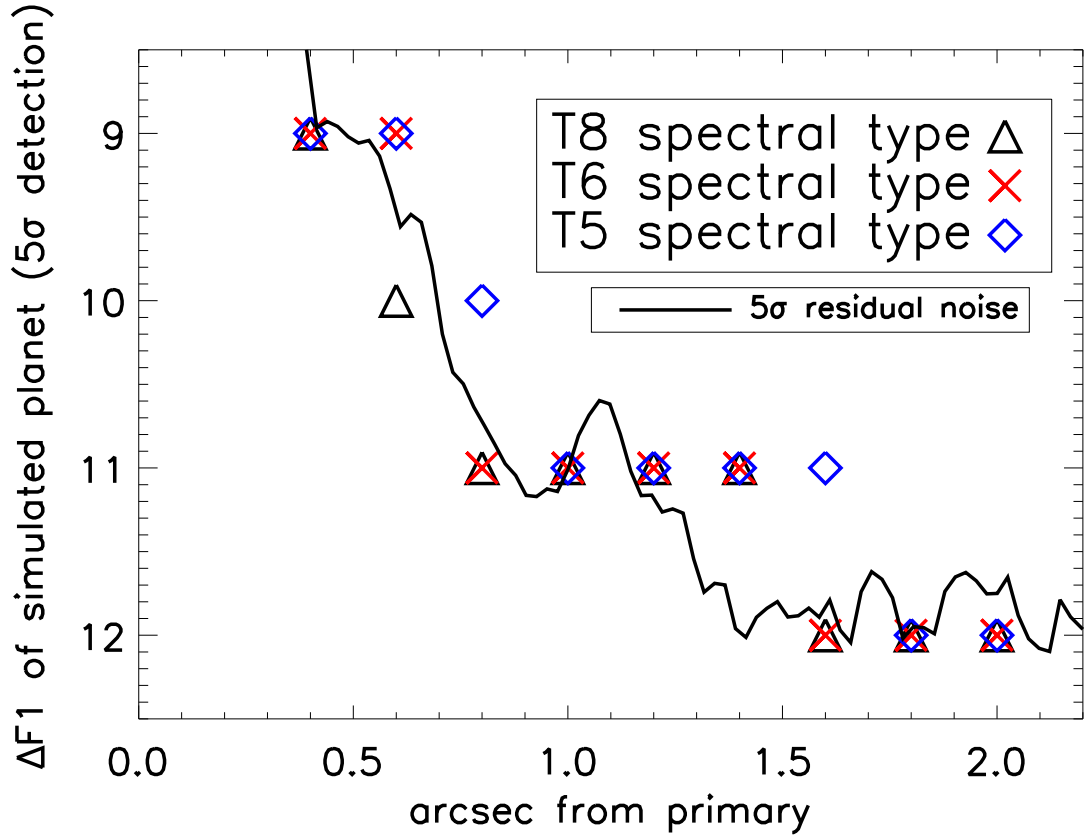


Fig. 20.— Maximum achievable planet contrast ( $5\sigma$  detection) vs. separation for 28 minutes of VLT SDI data for AB Dor A. To determine the maximum achievable planet contrast as a function of separation, we inserted and then attempted to retrieve simulated planets with a variety of separations and  $\Delta F1$  contrasts appropriate for T5, T6, and T8 spectral types. The residual SDI noise curve for AB Dor A is also overplotted; the two curves agree well, giving us confidence in our measured contrast limits.

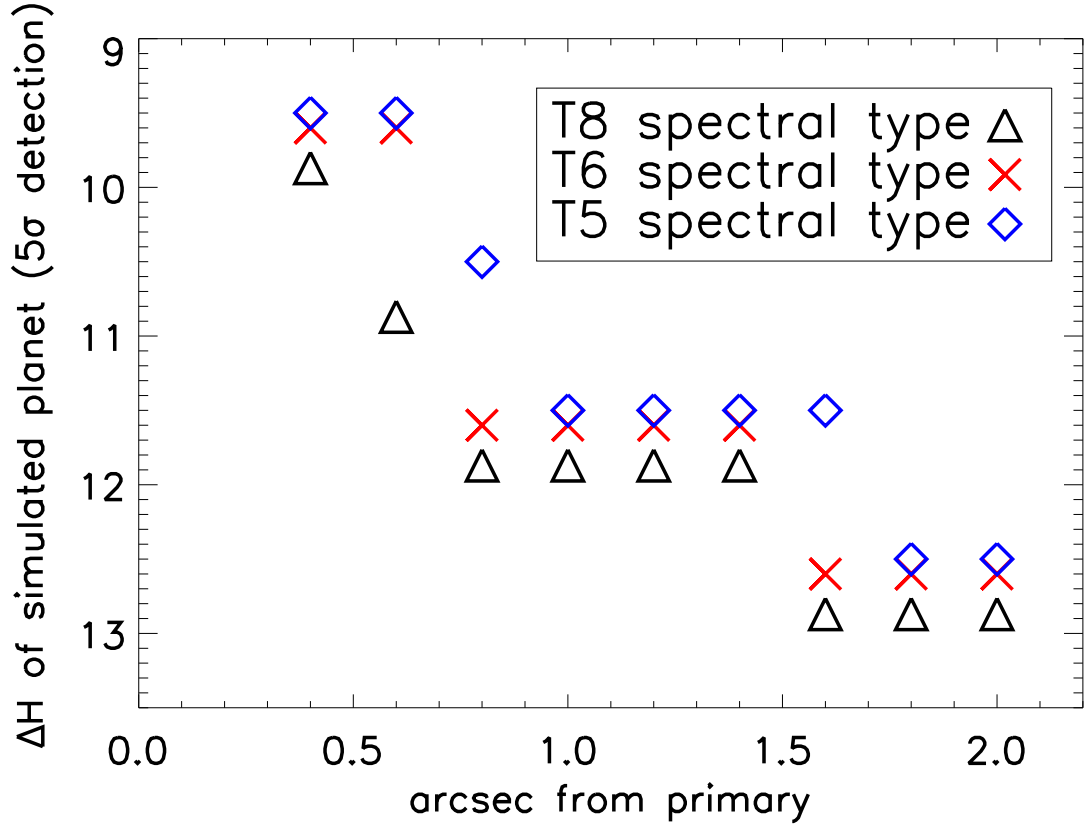


Fig. 21.— Maximum achievable H band planet contrast ( $5\sigma$  detection) vs. separation for 28 minutes of VLT SDI data for AB Dor A. To determine the maximum achievable planet contrast as a function of separation, we inserted and then attempted to retrieve simulated planets with a variety of separations and  $\Delta F1$  contrasts appropriate for T5, T6, and T8 spectral types.  $\Delta F1$  contrasts were converted to  $\Delta H$  magnitudes using the magnitude offsets calculated in section 3.3.

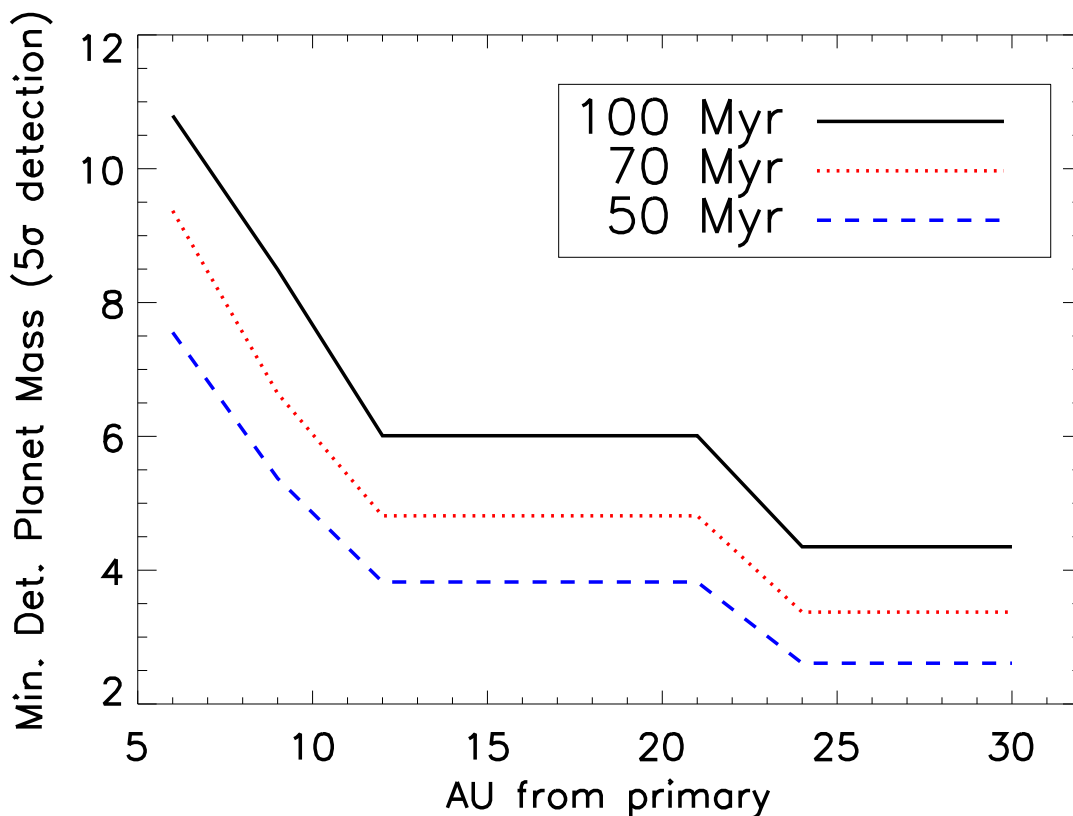


Fig. 22.— Minimum detectable planet mass ( $5\sigma$  detection) vs. separation (AU) for 28 minutes of VLT SDI data for AB Dor A. To determine the minimum detectable planet mass as a function of separation, we inserted and then attempted to retrieve simulated planets with a variety of separations and  $\Delta F1$  contrasts appropriate for T5, T6, and T8 spectral types.  $\Delta F1$  contrasts were converted to  $\Delta H$  magnitudes using the magnitude offsets calculated in section 3.3 and were then converted to absolute H magnitudes using the 2MASS apparent H magnitude and the Hipparcos distance for each star. Absolute H magnitudes were converted into planet masses using the models of Burrows et al. (2003) and adopting a range of system ages from 50 - 100 Myr. For AB Dor, we should be able to image ( $5\sigma$  detection) a  $5 M_{Jup}$  planet 12 AU from the star. For a complete set of minimum detectable planet mass vs. separation curves, see: <http://exoplanet.as.arizona.edu/~lclose/SDI.html>.

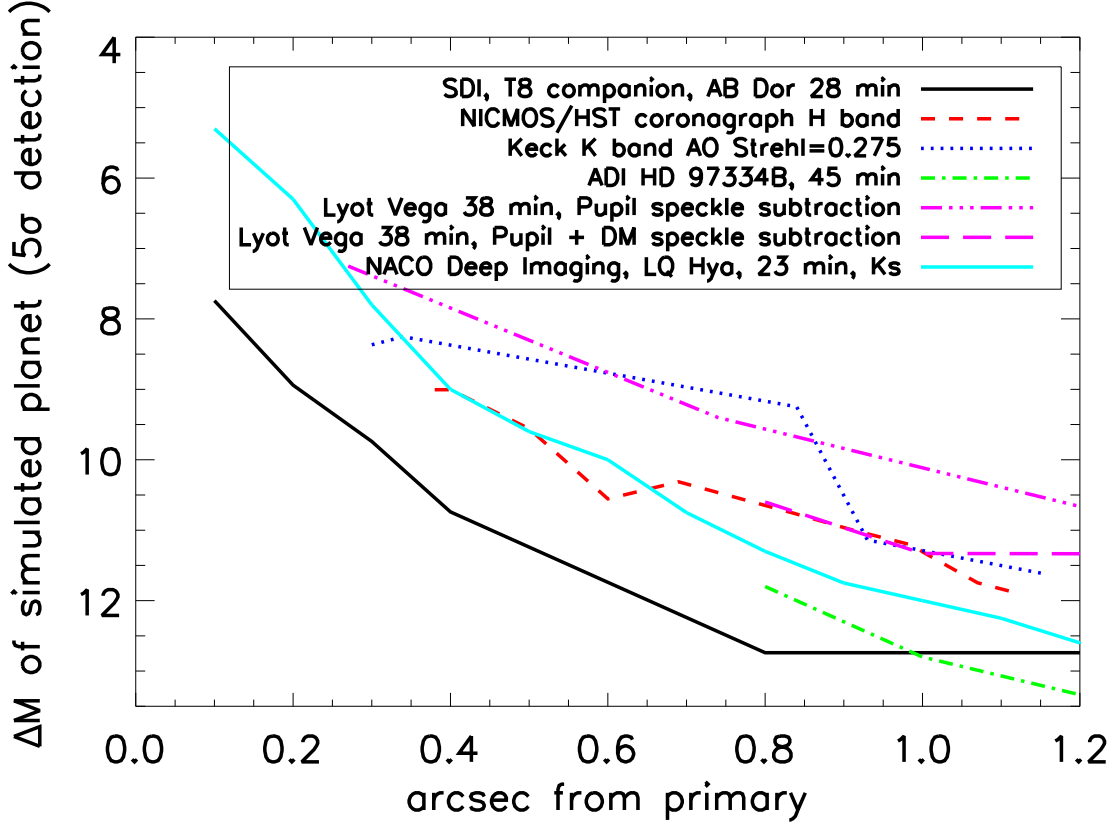


Fig. 23.— Comparison of SDI contrast curve with other methods. The Lyot curve is for the 3.6m AEOS telescope (Hinkley et al. 2007) and the NICMOS curve coronagraph curve is from HST (Schneider et al. 2003); otherwise curves are all from  $\geq 8$ m class telescopes. We use the LQ Hya contrast curve from Masciadri et al. (2005) because this star (K2, 18 pc vs. K1, 15 pc) is the closest match from that work to AB Dor A (our SDI comparison star.) The SDI contrast curve has been converted from  $\Delta F1=1.575\mu\text{m}$  to  $\Delta H$  contrasts appropriate for a T8 spectral type object. Inside  $0.4''$ , SDI contrasts are derived from the 1-trajectory SDI contrast plot of AB Dor A; outside of  $0.4''$ , SDI contrasts are derived from our in-depth planet simulation case study of AB Dor A. For methanated companions, SDI provides improved contrast by 1-4 mag within  $1''$  as compared to other methods. Past  $1''$ , narrowband imaging becomes less efficient and broad-band techniques (such as ADI; Marois et al. 2006) reach higher contrasts.

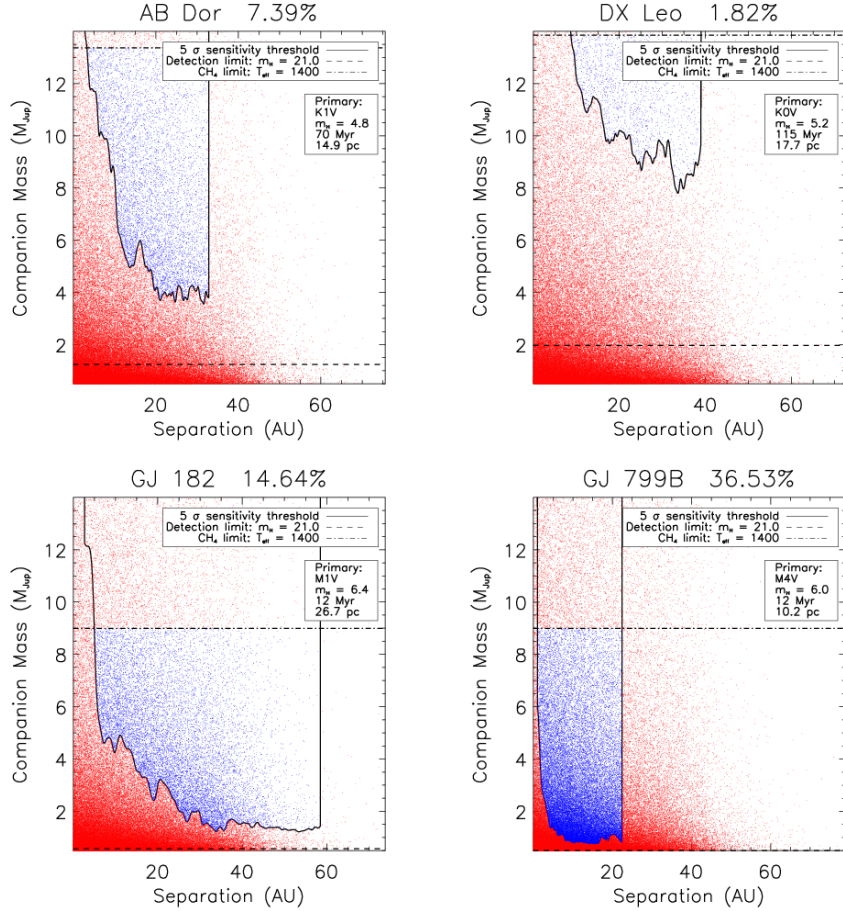


Fig. 24.— Minimum detectable mass vs. separation for a set of 4 typical program stars (upper left: AB Dor, upper right: DX Leo, lower left: GJ 182, lower right: GJ 799B). We convert our contrast curves in  $\Delta\text{mag}$  units (from Figs. 8 to 12) into minimum detectable mass vs. separation (in AU) using the models of Burrows et al. (2003) and the distance to the star. To characterize the possible planets we expect to detect around each star, we simulated an ensemble of  $10^6$  possible planets per star, assuming distributions for mass, eccentricity, and semi-major axis based on known radial velocity planets, as well as distributions for orbital phase and viewing angle. When combined with the properties of the individual target star and its measured contrast curve, we can determine what fraction of these simulated planets we expect to detect at the  $5\sigma$  level (shown above each plot with the name of the target star). The ensemble of simulated planets is shown as small dots for each star in; simulated planets which are detected with the contrast attained by SDI are plotted in blue and those that remain undetected are plotted in red. Assuming each star possesses exactly one planet, we can assign a detection probability for that star from the percentage of simulated planets detected. For our 48 program stars which possess contrast curves, the average detection probability is 8.0%, the median detection probability is 4.1%, and the maximum detection probability is 47%. For GJ 799B (12 Myr M star at 10 pc), we can detect (at  $5\sigma$ ) 5  $M_{Jup}$  planet at 2 AU.

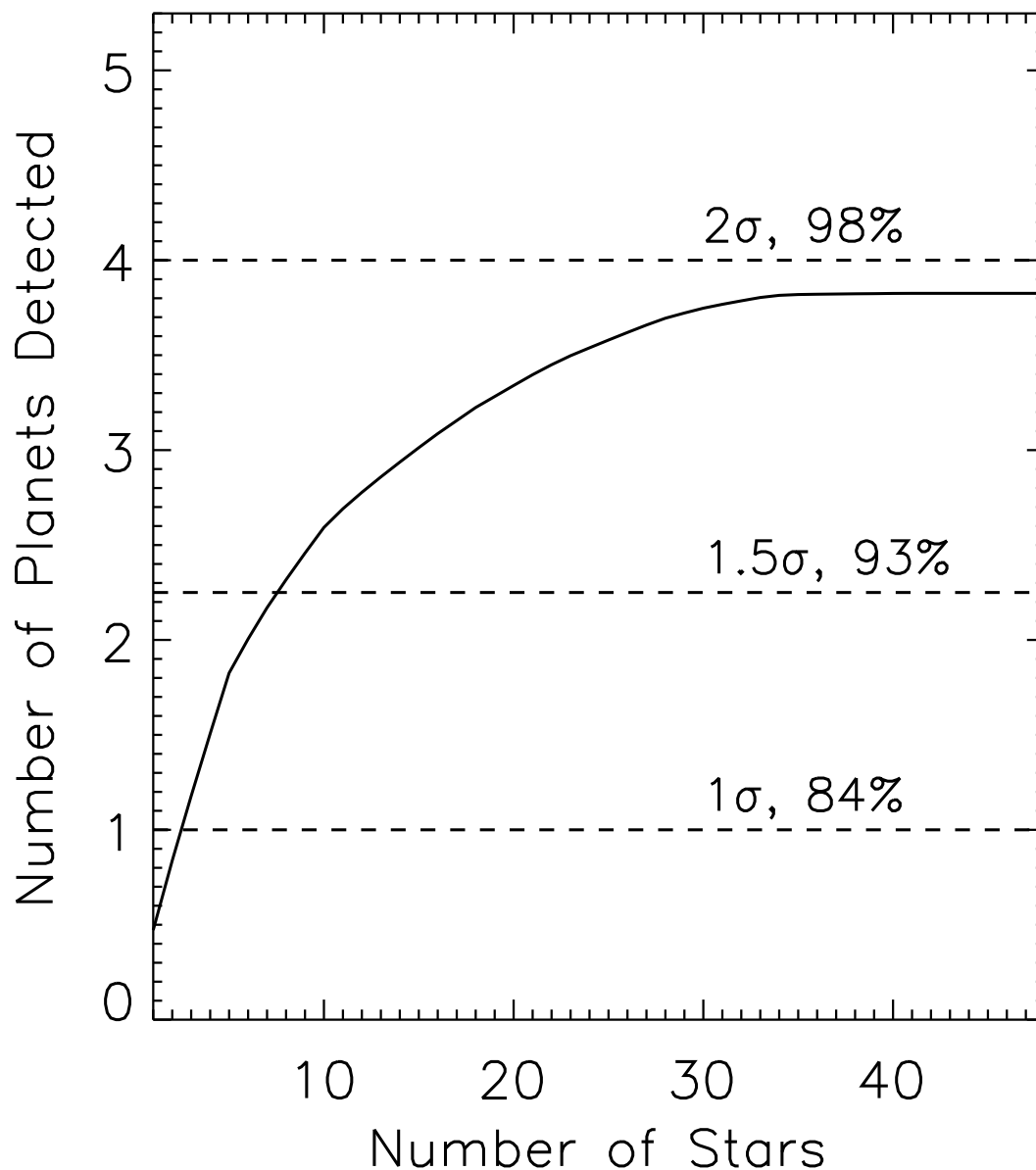


Fig. 25.— Expected number of planets detected. By taking the results of our Monte Carlo simulations, and assuming that each program star possesses exactly one planet, we can assign a detection probability for that star from the percentage of simulated planets detected. By adding these detection fractions for each star, we can compute the expected number of planets detected from our survey. We order the target stars by decreasing detection probability, and plot the total number of planets expected to be detected as a function of the number of stars. Over the entire survey, we expect to detect 3.8 planets, a  $2\sigma$  null result. Thus, our assumed distribution for the frequency (1 planet per star, hence 100%), semimajor axis distribution ( $N(a) \propto \text{constant}$ ), and luminosities (Burrows et al. 2003) of extrasolar planets is excluded at the 98% level by our extrasolar planet survey null result.

Table 1. Properties of SDI Survey Stars

Target	RA <sup>a</sup>	DEC	Distance(pc) <sup>a</sup>	SpT*	Age(Gyr) <sup>b</sup>	Age Ref <sup>b</sup>	V <sup>c</sup>	H <sup>d</sup>	Detectability	Comments
Nearby Young Stars										
HIP 1481	00 18 26.1	-63 28 39.0	41	F8/GOV <sup>e</sup>	0.03	Tuc	7.5	6.2	4.2%	
ERX6	01 23 21.2	-57 28 50.7	49.3	G6V <sup>e</sup>	0.03	Tuc/Hor	8.5	6.9	4.1%	
ERX8	01 28 08.7	-52 38 19.2	37.1	K1V <sup>e</sup>	0.03	Tuc/Hor	9.3	6.9	8.6%	
HIP 9141	01 57 48.9	-21 54 05.0	42.4	G3Ve/G5V <sup>f</sup>	0.03	Tuc/Hor	8.1	6.6	3.6%	poss. 0.15" binary
BD +05 378	02 41 25.9	+05 59 18.4	40.5	M0 <sup>g</sup>	0.012	Beta Pic	10	7.2	7.6%	
HD 17925	02 52 32.1	-12 46 11.0	10.4	K1V <sup>f</sup>	0.115	Possible Her/Lyr	6	4.2	5.7%	
LH98 062	03 24 06.5	+23 47 06.1	19.8	K4V <sup>h</sup>	0.1	Li from LH98	10	6.5		2.4" binary
V577 PerA	03 33 13.5	+46 15 26.5	33.8	G5IV/V <sup>j</sup>	0.07	AB Dor mg	8.3	6.5	2.0%	7" binary
V834 Tau	04 41 18.9	+20 54 05.4	13.5	K3V <sup>k</sup>	0.16	Li from WSH03	8.1	5.3	2.7%	
GJ 182	04 59 34.8	+01 47 00.7	26.7	M1Ve <sup>l</sup>	0.016	Li from FMS97	10	6.5	15%	very tentative planet candidate (4.8 AU, ~4 M <sub>Jup</sub> ) not detected at second epoch
HIP 23309	05 00 47.1	-57 15 25.5	26.3	M0/1 <sup>m</sup>	0.012	Beta Pic	10	6.4	16%	
AB Dor	05 28 44.8	-65 26 54.9	14.9	K1III <sup>c</sup>	0.07	AB Dor mg	6.9	4.8	7.4%	0.16" binary AB Dor C, Close et al. 2005
GJ 207.1	05 33 44.8	+01 56 43.4	16.8	M2.5e <sup>n</sup>	0.1	Lowrance et al. 2005	9.5	7.1	4.0%	
UY Pic	05 36 56.8	-47 57 52.9	23.9	K0V <sup>o</sup>	0.07	AB Dor mg	8	5.9	8.1%	
AO Men	06 18 28.2	-72 02 41.4	38.5	K6/7 <sup>m</sup>	0.012	Beta Pic	9.9	7	2.5%	very tentative planet candidate (14 AU, ~4 M <sub>Jup</sub> ) not detected at second epoch
HIP 30030	06 19 08.1	-03 26 20.0	52.4	G0V <sup>p</sup>	0.03	Tuc/Hor	8	6.6	0.2%	
AB Pic	06 19 12.9	-58 03 16.0	45.5	K2V <sup>e</sup>	0.03	Tuc	9.1	7.1	6.8%	planetary mass companion, Chauvin et al. 2005 very tentative planet candidate (15.5 AU, ~5 M <sub>Jup</sub> ) not detected at second epoch
SRX1	06 22 30.9	-60 13 07.1	23.5	G1V <sup>e</sup>	0.07	AB Dor	6.5	5.2	4.8%	
HD 48189A	06 38 00.4	-61 32 00.2	21.7	G1/G2V <sup>e</sup>	0.07	AB Dor	6.2	4.7	1.8%	0.14" binary
BD +23 1978	08 36 55.8	+23 14 48.0	41.6	K5V <sup>q</sup>	0.035	Montes et al. 2001	8.7	6.5		
π <sub>1</sub> UMa	08 39 11.7	+65 01 15.3	14.3	G1.5V <sup>q</sup>	0.21	Li from WSH03	5.6	4.3	0.1%	
LQ Hya	09 32 25.6	-11 11 04.7	18.3	K0V <sup>q</sup>	0.013	Li from WSH03	7.8	5.6	32%	
DX Leo	09 32 43.7	+26 59 18.7	17.7	K0V <sup>q</sup>	0.115	Her/Lyra	7	5.2	1.8%	very tentative planet candidate (2.6 AU, ~10 M <sub>Jup</sub> ) not detected at second epoch
TWA 22	10 17 26.9	-53 54 28.0	22	M5 <sup>g</sup>	0.01		14	8.1		
HD 92945	10 43 28.3	-29 03 51.4	21.6	K1V <sup>q</sup>	0.07	AB Dor	7.8	5.8	6.8%	very tentative planet candidate (10.4 AU, ~6 M <sub>Jup</sub> ) not detected at second epoch
GJ 417	11 12 32.4	+35 48 50.7	21.7	G0V <sup>r</sup>	0.115	Her/Lyra	6.4	5	0.0%	
TWA 4	11 22 05.3	-24 46 39.6	46.7	K4V <sup>t</sup>	0.01		9.1	5.8		0.78" binary
TWA 25	12 15 30.8	-39 48 42.0	44.1	M0 <sup>g</sup>	0.01	TW Hydra	11	7.5	14%	
RX J1224.8-7503	12 24 47.3	-75 03 09.4	24.2	K2 <sup>u</sup>	0.016	Li from AKCWM95	11	7.8	13.5%	
RX J1231.9-7848	12 31 56.0	-78 48 36.0	50	M1 <sup>u</sup>	0.01	Li from AKCWM95	14	9.6		
EK Dra	14 39 00.2	+64 17 30.0	33.9	G0 <sup>w</sup>	0.07	AB Dor	7.6	6	0.67%	binary, Metchev & Hillenbrand 2004
HD 135363	15 07 56.3	+76 12 02.7	29.4	G5V <sup>q</sup>	0.0032	Li from WSH03	8.7	6.3	5.2%	0.26" binary
KW Lup	15 45 47.6	-30 20 55.7	40.9	K2V <sup>v</sup>	0.002	Li from NB98	9.4	6.6	3.9%	
HD 155555AB	17 17 25.5	-66 57 04.0	30	G5IV+KOIV/V <sup>m</sup>	0.012	Beta Pic	7.2	4.9	0.06%	
HD 155555C	17 17 27.7	-66 57 00.0	30	M4.5 <sup>m</sup>	0.012	Beta Pic	13	7.9	47%	
HD 166435	18 09 21.4	+29 57 06.2	25.2	G0 <sup>x</sup>	0.1	RHK from Wright+ 04	6.8	5.4	1.1%	



Table 1—Continued

Target	RA <sup>a</sup>	DEC	Distance(pc) <sup>a</sup>	SpT*	Age(Gyr) <sup>b</sup>	Age Ref <sup>b</sup>	V <sup>c</sup>	H <sup>d</sup>	Detectability	Comments
HD 172555A	18 45 26.9	-64 52 16.5	30	A5IV/V <sup>e</sup>	0.012	Beta Pic	4.8	4.3	5.8%	
CD-64 1208	18 45 37.0	-64 51 44.6	29.2	K7 <sup>m</sup>	0.012	Beta Pic	10	6.3	9.9%	0.18" binary
HD 181321	19 21 29.8	-34 59 00.5	20	G1/G2V <sup>v</sup>	0.16	Li from WSH03, RHK from Gray+ 06	6.5	5	0.09%	very tentative planet candidate (7 AU, $\sim 5 M_{Jup}$ ) not detected at second epoch
HD 186704	19 45 57.3	+04 14 54.6	30.3	G0 <sup>x</sup>	0.2	RHK from Wright+ 04	7	5.6	0.0%	
GJ 799B	20 41 51.1	-32 26 09.0	10.2	M4.5e <sup>n</sup>	0.012	Beta Pic	13	—	36%	
GJ 799A	20 41 51.2	-32 26 06.6	10.2	M4.5e <sup>n</sup>	0.012	Beta Pic	11	5.2	18%	
GJ 803	20 45 09.5	-31 20 27.1	9.94	M0Ve <sup>n</sup>	0.012	Beta Pic	8.8	4.8	33%	very tentative planet candidate (3 AU, $\sim 2 M_{Jup}$ ) not detected at second epoch
HIP 112312A	22 44 57.8	-33 15 01.0	23.6	M4e <sup>g</sup>	0.012	Beta Pic	12	7.2	34%	very tentative planet candidate (6.2 AU, $\sim 8 M_{Jup}$ ) not detected at second epoch
HD 224228	23 56 10.7	-39 03 08.4	22.1	K3V <sup>v</sup>	0.07	AB Dor	8.2	6	5.8%	
More Distant Young Stars										
TWA 14	11 13 26.5	-45 23 43.0	66.7	M0 <sup>h</sup>	0.01	TW Hydra	13	8.7	7.8%	
RXJ 1243.6-7834	12 43 36.7	-78 34 07.8	150	M0 <sup>h</sup>	0.008	Li from AKCWM95	13	8.7		0.068" binary
Stars with known RV planets										
$\epsilon$ Eri	03 32 55.8	-09 27 29.7	3.22	K2V <sup>1</sup>	0.8	Benedict et al. 2006		1.9	0.1%	Kellner et al. 2007, Janson et al. 2007
HD 81040	09 23 47.1	+20 21 52.0	32.6	G0V <sup>q</sup>	2.5	Li from SUZT06	7.7	6.3	0.0%	
HD 128311	14 36 00.6	+09 44 47.5	16.6	K0 <sup>q</sup>	0.63	RHK from Gray+ 03	7.5	5.3	0.0%	
Nearby Solar Analogues										
HD 114613	13 12 03.2	-37 48 10.9	20.5	G3V <sup>v</sup>	4.2	Li from RGP93, RHK from Gray+06	4.8	3.3	0.0%	
HD 201091	21 06 53.9	+38 44 57.9	3.48	K5Ve <sup>n</sup>	2.0 <sup>1</sup>	RHK from Gray+ 06	5.2	2.5	0.0%	
$\epsilon$ Ind A	22 03 21.7	-56 47 09.5	3.63	K4.5V <sup>n</sup>	1.3	Lachaume et al. 1999	4.7	2.3	0.09%	Geißler et al. 2007
GJ 862	22 29 15.2	-30 01 06.4	15.4	K5Ve <sup>n</sup>	6.3 <sup>1</sup>	RHK from Gray+ 06	7.7	5.3	0.0%	

<sup>1</sup>In general, we have only determined Ca R'HK ages for stars with spectral types K1 or earlier, but in the case of these two K5 stars, we have only the R'HK measurement on which to rely for age determination. The calibration of Mt. Wilson S-index to R'HK for K5 stars (B-V  $\sim 1.1$  mag) has not been well-defined (Noyes et al. 1984; specifically the photospheric subtraction), and hence applying a R'HK vs. age relation for K5 stars is unlikely to yield useful ages. Although we adopt specific values for the ages of these stars, it would be more accurate to state simply that these stars have ages

>1 Gyr. As a result, almost all simulated planets are too faint to detect around these stars, so the precise error in the age does not significantly affect our final results.

<sup>a</sup>derived from the Hipparcos survey, Perryman et al.(1997)

<sup>b</sup>ages for stars with cluster memberships from Zuckerman and Song (2004), otherwise, ages are either lithium ages, calcium RHK ages, or an average of both. Acronyms for lithium and calcium age references: AKCWM95: Alcalá, Krautter, Schmitt, Covino, Wichmann, and Mundt 1995, FMS97: Favata, Micela, and Sciortino 1997, LH98: Li and Hu 1998, NB98: Neuhauser and Brandner 1998, RGP93: Randich, Gratton, and Pallavicini 1993, SUZT06: Sozzetti, Udry, Zucker, Torres, Beuzit, et al. 2006, WSH03: Wichmann, Schmitt, and Hubrig 2003

<sup>c</sup>from the CDS Simbad service

<sup>d</sup>from the 2MASS Survey, Cutri et al. (2003)

\*Spectral reference key: e: Houk and Cowley 1975, f: Houk and Cowley 1988,

g: Zuckerman and Song 2004, h: Li and Hu 1998, i: Cowley, Hiltner, and Witt 1967,

j: Christian and Mathioudakis 2002, k: Leaton and Pagel 1960, l: Favata, Barbera, Micela, and Sciortino 1995,

m: Zuckerman, Song, Bessell, and Webb 2001, n: Gliesse and Jahrei 1991, o: Houk 1978,  
p: Cutispoto, Pallavicini, Kuerster, and Rodono 1995,  
q: Montes, Lopez-Santiago, Galvez, Fernandez-Figueroa, De Castro, and Cornide 2001,  
r: Bidelman 1951, s: Zuckerman, Webb, Schwartz, and Becklin 2001, t: Houk and Smith-Moore 1988,  
u: Alcal, Krautter, Schmitt, Covino, Wichmann, and Mundt 1995, v: Houk 1982,  
w: Gliesse and Jahrei 1979, x: Henry Draper Catalog

Table 2. VLT SDI Observation Log

Object	Date	DIT	NDIT	Total Exp (minutes)
HIP 1481	2004-11-15	14	6	56
	2005-11-24	16	5	26.7
	2005-11-25	16	5	26.7
	2005-11-27	16	5	26.7
ERX6	2004-11-14	22	4	29.3
	2004-11-16	22	4	58.7
ERX8	2004-11-17	22	4	58.7
HIP9141	2004-09-27	14	6	56
BD +05 378	2005-02-01	32	3	25.6
HD 17925	2003-08-14	7.5	16	40
	2003-08-16	4	30	40
	2003-08-17	4	30	20
	2004-02-02	1	120	20
	2004-11-16	4.1	17	46.5
	2004-11-17	4.1	17	46.5
LH98 062	2004-02-03	14	9	21
$\epsilon$ Eri	2004-09-19	0.6	160	64
V834 Tau	2005-01-25	10	9	24
	2005-02-01	10	9	24
GJ 182	2004-02-02	7	17	39.7
	2005-11-22	20	4	26.7
	2005-11-24	20	4	26.7
	2005-11-27	20	4	26.7
HIP23309	2005-01-30	24	4	25.6
	2005-01-31	24	4	51.2
AB Dor	2004-02-02	5	24	20
	2004-09-28	12	7	28
	2004-11-16	10.4	8	27.7
GJ 207.1	2005-01-27	32	3	25.6
UY Pic	2004-11-16	14	6	28
	2004-11-17	14	6	56

Table 2—Continued

Object	Date	DIT	NDIT	Total Exp (minutes)
AO Men	2004-02-03	14	9	21
	2005-11-15	30	1	17.5
	2005-11-24	30	1	10
AB Pic	2004-11-14	20	4	26.7
	2004-11-15	20	4	26.7
	2005-11-22	20	4	13.3
	2005-11-25	20	4	53.3
SRX1	2004-11-18	12	7	28
	2004-11-19	12	7	28
HD 48189A	2004-11-17	6.5	11	23.8
	2004-11-18	6.5	11	23.8
BD +23 1978	2005-01-27	24	4	25.6
	2005-01-28	24	4	25.6
LQ Hya	2004-02-02	5	24	40
	2004-12-08	14	6	28
	2004-12-14	14	6	28
DX Leo	2004-02-05	3	38	19
	2005-12-04	14	6	28
	2005-12-19	14	6	28
TWA 22	2005-01-25	32	1	48.5
HD92945	2004-02-05	5	24	60
TWA 14	2005-01-28	32	3	25.6
	2005-01-29	32	3	25.6
TWA 4	2004-02-02	7	17	9.92
TWA25	2005-01-28	32	3	25.6
RX J1224.8-7503	2004-02-02	40	3	20
	2005-01-16	30	3	60
	2005-01-27	30	3	120
RX J1231.9-7848	2004-02-05	20	6	20
RXJ 1243.6-7834	2004-02-02	5	24	40
HD 114613	2004-02-02	1	120	40

Table 2—Continued

Object	Date	DIT	NDIT	Total Exp (minutes)
KW Lup	2004-09-15	22	4	14.7
	2004-09-16	24	4	22.7
	2004-09-17	24	4	24
HD155555AB	2003-08-14	7.5	16	10
	2003-08-15	7.5	16	20
	2003-08-16	7.5	16	10
	2003-08-17	7.5	16	10
	2004-09-16	10	9	30
	2004-09-18	14	6	28
HD155555C	2003-08-14	30	4	40
	2003-08-16	30	4	40
HD172555A	2003-08-17	5	24	20
	2004-09-17	5	15	25
	2004-09-18	5	15	6.25
	2004-09-19	5	15	18.8
CD-64 1208	2003-08-17	20	6	40
	2004-09-16	15	6	30
HD181321	2003-08-15	7.5	16	40
	2004-09-18	11	8	29.3
GJ799B	2003-08-16	20	6	40
	2003-08-17	20	6	30
	2004-09-19	15	6	30
GJ799A	2003-08-16	20	6	40
	2004-09-16	10	9	30
	2004-09-19	15	6	30
GJ803	2003-08-14	7.5	18	56.2
	2003-08-15	10	12	40
	2003-08-17	7.5	16	40
	2004-09-17	6	15	30
	2004-09-18	10	9	30
$\epsilon$ Ind A	2004-09-18	0.5	192	48

Table 2—Continued

Object	Date	DIT	NDIT	Total Exp (minutes)
GJ 862	2003-08-15	10	12	40
	2003-08-16	10	12	40
	2004-09-19	13	7	48.2
HIP112312A	2004-09-19	25	4	66.7
HD224228	2003-08-16	10	12	40
	2003-08-17	20	6	40
	2004-10-08	14	6	28
	2004-10-20	21	4	28

Table 3. MMT SDI Observation Log

Object	Date	DIT	NDIT	Total Exp (minutes)
V577 PerA	2006-02-12	20	7	37.3
	2006-02-13	21.5	7	40.1
HIP30030	2006-02-12	30	5	30
$\pi_1$ UMa	2006-02-13	5.8	13	40.2
HD 81040	2006-02-12	11.7	13	40.3
LQ Hya	2006-02-12	8	19	40.5
DX Leo	2005-05-01	10	13	34.7
GJ 417	2005-04-30	7	17	31.7
HD 128311	2006-02-12	4	19	60.8
EK Dra	2005-05-01	20	7	37.3
HD 135363	2005-05-01	30	5	40
HD 166435	2005-04-30	7	17	31.7
	2005-05-01	7	17	31.7
HD 186704	2005-05-01	10	13	17.3
HD 201091	2005-04-30	20	7	37.33

Table 4. Limiting H mag ( $5\sigma$ ) at  $0.5''$

Object	$\Delta F1$	Separation(AU)	$\Delta H$ (T8 SpT)	$m_H$	$M_H$
$\epsilon$ Eri	$9.4 \pm 0.12$	1.61	10.3	12.2	14.7
$\epsilon$ Ind A	$10.6 \pm 0.12$	1.81	11.5	13.8	16
HD 201091	$8.08 \pm 0.52$	1.74	8.95	11.5	13.8
HD 114613	$6.13 \pm 0.26$	10.2	7	10.3	8.74
HD 17925	$9.69 \pm 0.14$	5.19	10.6	14.8	14.7
HD172555A	$9.14 \pm 0.12$	15	10	14.3	11.9
$\pi_1$ UMa	$8.04 \pm 0.15$	7.14	8.91	13.2	12.4
HD 48189A	$8.54 \pm 0.052$	10.8	9.41	14.2	12.5
GJ803	$9.54 \pm 0.091$	4.97	10.4	15.2	15.2
AB Dor	$9.04 \pm 0.019$	7.47	9.91	14.8	13.9
HD155555AB	$5.87 \pm 0.14$	15	6.74	11.6	9.21
GJ 417	$7.79 \pm 0.23$	10.9	8.66	13.7	12
HD181321	$7.42 \pm 0.13$	10	8.29	13.3	11.8
SRX1	$9.95 \pm 0.079$	11.7	10.8	16	14.1
GJ799A	$7.48 \pm 0.082$	5.11	8.35	13.6	13.6
DX Leo	$8.24 \pm 0.19$	8.87	9.11	14.4	13.2
GJ 862	$9.51 \pm 0.25$	7.72	10.4	15.7	14.8
V834 Tau	$9.08 \pm 0.18$	6.74	9.95	15.3	14.6
HD 166435	$8.42 \pm 0.17$	12.6	9.29	14.7	12.7
LQ Hya	$9.82 \pm 0.16$	9.17	10.7	16.3	15
HD 186704	$7.13 \pm 0.091$	15.1	8	13.6	11.2
HD92945	$9.91 \pm 0.0099$	10.8	10.8	16.6	14.9
UY Pic	$9.96 \pm 0.11$	11.9	10.8	16.7	14.8
HD224228	$9 \pm 0.15$	11	9.87	15.9	14.2
EK Dra	$7.85 \pm 0.39$	17	8.72	14.7	12
HIP 1481	$9.22 \pm 0.13$	20.5	10.1	16.3	13.2
CD-64 1208	$9.33 \pm 0.087$	14.6	10.2	16.5	14.2
HD 135363	$7.9 \pm 0.27$	14.7	8.77	15.1	12.8
HIP23309	$8.45 \pm 0.092$	13.1	9.32	15.7	13.6
GJ 182	$8.01 \pm 0.16$	13.3	8.88	15.3	13.2
V577 PerA	$8.9 \pm 0.33$	16.9	9.77	16.2	13.6



Table 4—Continued

Object	$\Delta F1$	Separation(AU)	$\Delta H$ (T8 SpT)	$m_H$	$M_H$
HIP9141	$8.92 \pm 0.29$	21.2	9.79	16.3	13.2
HIP30030	$6.91 \pm 0.17$	26.2	7.78	14.4	10.8
KW Lup	$8.76 \pm 0.091$	20.5	9.63	16.3	13.2
ERX8	$9.4 \pm 0.2$	18.6	10.3	17.2	14.4
ERX6	$9.38 \pm 0.4$	24.6	10.2	17.1	13.6
AO Men	$6.91 \pm 0.33$	19.2	7.78	14.8	11.9
AB Pic	$9.65 \pm 0.027$	22.8	10.5	17.6	14.3
GJ 207.1	$7.5 \pm 0.094$	8.41	8.37	15.5	14.4
HIP112312A	$9.09 \pm 0.27$	11.8	9.96	17.1	15.2
BD +05 378	$8.31 \pm 0.088$	20.3	9.18	16.4	13.4
TWA25	$9.5 \pm 0.035$	22	10.4	17.9	14.7
RX J1224.8-7503	$7.16 \pm 0.024$	12.1	8.03	15.9	14
HD155555C	$10.5 \pm 0.085$	15	11.4	19.3	16.9
TWA 14	$8.38 \pm 0.03$	33.3	9.25	18	13.9

Table 5. Limiting H mag ( $5\sigma$ ) at  $1.0''$

Object	$\Delta F1$	Separation(AU)	$\Delta H$ (T8 SpT)	$m_H$	$M_H$
$\epsilon$ Eri	$11.3 \pm 0.2$	3.22	12.2	14.1	16.6
$\epsilon$ Ind A	$12 \pm 0.16$	3.63	12.9	15.2	17.4
HD 201091	$9.42 \pm 0.05$	3.48	10.3	12.8	15.1
HD 114613	$7.24 \pm 0.13$	20.5	8.11	11.5	9.94
HD 17925	$11.3 \pm 0.19$	10.4	12.2	16.4	16.3
HD172555A	$11.2 \pm 0.098$	30	12.1	16.4	14
$\pi_1$ UMa	$9.28 \pm 0.14$	14.3	10.1	14.4	13.6
HD 48189A	$9.87 \pm 0.24$	21.7	10.7	15.4	13.7
GJ803	$10.7 \pm 0.03$	9.94	11.6	16.4	16.4
AB Dor	$11 \pm 0.17$	14.9	11.9	16.7	15.8
HD155555AB	$7.3 \pm 0.046$	30	8.17	13.1	10.7
GJ 417	$8.44 \pm 0.05$	21.7	9.31	14.3	12.6
HD181321	$8.63 \pm 0.048$	20	9.5	14.6	13.1
SRX1	$11.2 \pm 0.13$	23.5	12.1	17.3	15.4
GJ799A	$9.55 \pm 0.14$	10.2	10.4	15.6	15.6
DX Leo	$9.98 \pm 0.039$	17.7	10.8	16	14.8
GJ 862	$10.7 \pm 0.12$	15.4	11.6	16.9	16
V834 Tau	$10.2 \pm 0.18$	13.5	11.1	16.4	15.7
HD 166435	$9.98 \pm 0.061$	25.2	10.8	16.2	14.2
LQ Hya	$11 \pm 0.035$	18.3	11.9	17.5	16.2
HD 186704	$7.35 \pm 0.052$	30.3	8.22	13.8	11.4
HD92945	$10.8 \pm 0.062$	21.6	11.7	17.5	15.8
UY Pic	$11.5 \pm 0.033$	23.9	12.4	18.3	16.4
HD224228	$10.8 \pm 0.11$	22.1	11.7	17.7	16
EK Dra	$8.86 \pm 0.14$	33.9	9.73	15.7	13
HIP 1481	$10.8 \pm 0.046$	41	11.7	17.9	14.8
CD-64 1208	$9.88 \pm 0.54$	29.2	10.8	17.1	14.8
HD 135363	$8.65 \pm 0.025$	29.4	9.52	15.8	13.5
HIP23309	$10 \pm 0.051$	26.3	10.9	17.3	15.2
GJ 182	$10.2 \pm 0.15$	26.7	11.1	17.6	15.5
V577 PerA	$10 \pm 0.062$	33.8	10.9	17.4	14.8

Table 5—Continued

Object	$\Delta F1$	Separation(AU)	$\Delta H$ (T8 SpT)	$m_H$	$M_H$
HIP9141	$10.5 \pm 0.028$	42.4	11.4	18	14.9
HIP30030	$8.3 \pm 0.09$	52.4	9.17	15.8	12.2
KW Lup	$9.86 \pm 0.17$	40.9	10.7	17.3	14.2
ERX8	$10.7 \pm 0.12$	37.1	11.6	18.5	15.7
ERX6	$10.6 \pm 0.12$	49.3	11.5	18.4	14.9
AO Men	$7.9 \pm 0.015$	38.5	8.77	15.8	12.9
AB Pic	$10.8 \pm 0.013$	45.5	11.7	18.8	15.5
GJ 207.1	$8.74 \pm 0.089$	16.8	9.61	16.8	15.7
HIP112312A	$10.6 \pm 0.068$	23.6	11.5	18.7	16.8
BD +05 378	$9.52 \pm 0.074$	40.5	10.4	17.6	14.6
TWA25	$10.5 \pm 0.18$	44.1	11.4	18.9	15.7
RX J1224.8-7503	$8.04 \pm 0.16$	24.2	8.91	16.8	14.9
HD155555C	$10.8 \pm 0.043$	30	11.7	19.6	17.2
TWA 14	$8.74 \pm 0.047$	66.7	9.61	18.3	14.2

Table 6. Star/Planet Projected Minimum Detectable Separations for 5 and 10  $M_{Jup}$  Planets

Object	Age (Myr)	Distance (pc)	Separation 5 $M_{Jup}$ (AU)		Separation 10 $M_{Jup}$ (AU)	
			Burrows et al.	Baraffe et al.	Burrows et al.	Baraffe et al.
AB Dor	70	14.94	13.45	20.92	6.28	10.31
AO Men	12	38.48	30.01	—*	11.54	20.01
BD+05 378	12	40.54	16.21	28.37	7.70	9.32
CD -64 1208	12	34.21	11.29	17.45	5.82	8.55
DX Leo	115	17.75	—	—	16.68	33.54
EK Dra	70	33.94	—	—	—	—
$\epsilon$ Eri	800	3.22	—	—	—	—
$\epsilon$ Ind A	1300	3.63	—	—	—	3.81
GJ 174	160	13.49	—	—	12.01	17.54
GJ 182	12	26.67	6.67	16.27	4.80	5.60
GJ 207.1	100	16.82	—	—	10.77	15.48
GJ 417	115	21.72	—	—	—	—
GJ 799A	12	10.22	1.94	4.60	1.12	1.64
GJ 799B	12	10.22	1.43	1.94	1.12	1.12
GJ 803	12	9.94	1.39	2.39	1.09	1.09
GJ 862	6300	15.45	—	—	—	—
HD 114613	4200	20.48	—	—	—	—
HD 128311	630	16.57	—	—	—	—
HD 135363	3	29.44	8.54	11.78	3.24	6.77
HD 155555 AB	12	30.03	—	—	25.23	—
HD 155555 C	12	30.03	3.30	3.30	3.30	3.30
HD 166435	100	25.24	—	—	29.03	—

Table 6—Continued

Object	Age (Myr)	Distance (pc)	Separation 5 $M_{Jup}$	(AU)	Separation 10 $M_{Jup}$	(AU)
HD 172555 A	12	29.23	20.17	28.65	6.43	14.62
HD 17925	115	10.38	14.43	—	5.40	8.62
HD 181321	160	20.86	—	—	—	—
HD 201091	2000	3.48	—	—	—	—
HD 224228	70	22.08	22.31	—	9.50	13.69
HD 45270	70	23.50	30.78	—	10.57	15.98
HD 48189 A	70	21.67	—	—	19.93	27.95
HD 81040	2500	32.56	—	—	—	—
HD 8558	30	49.29	27.11	67.52	11.34	22.18
HD 186704	200	30.26	—	—	—	—
HD 9054	30	37.15	19.32	31.20	7.06	9.29
HD 92945	70	21.57	24.59	44.00	6.04	10.14
HIP 112312 A	12	23.61	3.54	5.19	2.60	2.83
HIP 1481	30	40.95	30.71	59.38	12.69	20.88
HIP 23309	12	26.26	6.83	16.02	2.89	4.99
HIP 30030	30	52.36	—	—	53.93	—
AB Pic	30	45.52	19.12	40.05	9.56	13.65
HIP 9141	30	42.35	37.70	78.78	15.25	22.45
KW Lup	2	40.92	6.14	7.36	4.50	4.50
LQ Hya	13	18.34	3.30	4.95	2.02	2.75
RXJ1224.8-7503	16	24.17	6.53	17.16	3.63	4.59
TWA 14	10	66.67	14.00	27.33	7.33	10.67
TWA 25	10	44.05	9.25	14.10	4.85	7.93

Table 6—Continued

Object	Age (Myr)	Distance (pc)	Separation 5 $M_{Jup}$	(AU)	Separation 10 $M_{Jup}$	(AU)
UY Pic	70	23.87	19.81	29.12	5.73	11.46
V577 Per A	70	33.77	81.73	—	17.90	27.02
$\pi_1$ UMa	210	14.27	—	—	—	—

\*— means that such an object is too low in mass to be detected with our current survey contrast level for that star

Table 7. Binary Properties

Object	Separation	Position Angle
SDI survey discoveries		
AB Dor AC <sup>a</sup>	0.16''	127°
HIP 9141	0.15''	355°
HD 48189AC	0.14''	143°
HD 135363	0.26''	132°
CD -64 1208	0.18''	95°
SDI survey confirmations		
RXJ 1243.6-7834 <sup>b</sup>	0.068''	171°/351°
LH 98 062	2.4''	354°
TWA 4	0.78''	3°
EK Dra	0.67''	176°

<sup>a</sup>Separation and position angle from Close et al. 2005b. For updated photometry and astrometry see Close et al. 2007b.

<sup>b</sup>As RXJ 1243.6-7834 is nearly an equal-magnitude binary, we were unable to determine which star was the primary (as selected by Brandner et al. (2000)) and thus present two values for the position angle (assuming each star is the primary in turn).

## REFERENCES

- Alcala, J. M., Krautter, J., Schmitt, J. H. M. M., Covino, E., Wichmann, R., & Mundt, R. 1995, *A&AS*, 114, 109
- Baraffe, I., Chabrier, G., Barman, T.S., Allard, F., & Hauschildt, P.H. 2003, *A&A*, 402, 701
- Benedict, G. F., et al. 2006, *AJ*, 132, 2206
- Berton et al. 2006, *PASP*, 118, 1144
- Bidelman, W. P. 1951, *ApJ*, 113, 304
- Biller, B. A., Close, L. M., Lenzen, R., Brandner, W., McCarthy, D., Nielsen, E., Kellner, S., & Hartung, M. 2006, *IAU Colloq. 200: Direct Imaging of Exoplanets: Science & Techniques*, 571
- Biller, B.A., Kasper, M., Close, L.M., Brandner, W., & Kellner, S. 2006, *ApJ*, 641, L141
- Biller, B. A., et al. 2006, *Proc. SPIE*, 6272, 74
- Brandeker, A., Jayawardhana, R., Ivanov, V. D., & Kurtev, R. 2006, *ApJ*, 653, L61
- Brandner et al. 2000, *AJ*, 120, 950
- Boss, A. P. 2003, *ApJ*, 599, 577
- Burgasser, A. 2001, *Caltech PhD Thesis*
- Burgasser, A. et al. 2003, *AJ*, 125, 850
- Burrows, A., Hubbard, W. B., Lunine, J. I., & Liebert, J. 2001, *Reviews of Modern Physics*, 73, 719
- Burrows, A., Sudarsky, D. & Lunine, J. 2003, *ApJ*, 596, 587
- Butler, R. P., et al. 2006, *ApJ*, 646, 505
- Chauvin, G., Lagrange, A.-M., Dumas, C., Zuckerman, B., Mouillet, D., Song, I., Beuzit, J.-L., & Lowrance, P. 2005, *A&A*, 438, L25
- Chauvin, G., et al. 2005, *A&A*, 438, L29
- Christian, D. J., & Mathioudakis, M. 2002, *AJ*, 123, 2796



- Close, L.M., Lenzen, R., Biller, B.A., Brandner, W. & Hartung, M. 2005, Science with AO ESO Workshop, 136
- Close, L.M. et al. 2005, Nature, 433, 286
- Close, L.M. 2007, ApJ in press, astro-ph/0608574
- Close, L.M. 2007, ApJ in press, astro-ph/0703564
- Codona, J. L., & Angel, R. 2004, ApJ, 604, L117
- Cowley, A. P., Hiltner, W. A., & Witt, A. N. 1967, AJ, 72, 1334
- Cruz, K.L., Reid, N.I., Liebert, J., Kirkpatrick, J.D., & Lowrance, P.J. 2003, AJ, 126, 2421
- Cutispoto, G., Pallavicini, R., Kuerster, M., & Rodono, M. 1995, A&A, 297, 764
- Cutri, R.M. et al. 2003, 2MASS All-Sky Catalog of Point Sources
- Dohlen, K., Beuzit, J.-L., Feldt, M., Mouillet, D., Puget, P., Antichi, J., Baruffolo, A., Baudoz, P., Berton, A., Boccaletti, A., Carbillet, M., Charton, J., Claudi, R., Downing, M., Fabron, C., Feautrier, P., Fedrigo, E., Fusco, T., Gach, J.-L., Gratton, R., Hubin, N., Kasper, M., Langlois, M., Longmore, A., Moutou, C., Petit, C., Pragt, J., Rabou, P., Rousset, G., Saisse, M., Schmid, H.-M., Stadler, E., Stamm, D., Turatto, M., Waters, R., & Wildi, F. 2006, Proc. SPIE, 6269, 24
- Favata, F., Barbera, M., Micela, G., & Sciortino, S. 1995, A&A, 295, 147
- Favata, F., Micela, G., & Sciortino, S. 1997, A&A, 326, 647
- Fischer, D. A., & Valenti, J. 2005, ApJ, 622, 1102
- Geballe, T.R. et al. 2002, ApJ, 564, 466
- Geißler, K., et al. 2007, A&A, 461, 665
- Gliese, W., & Jahreiß, H. 1979, A&AS, 38, 423
- Gliese, W., & Jahreiß, H. 1991, On: The Astronomical Data Center CD-ROM: Selected Astronomical Catalogs, Vol. I; L.E. Brodzmann, S.E. Gesser (eds.), NASA/Astronomical Data Center, Goddard Space Flight Center, Greenbelt, MD
- Gray, R. O., Corbally, C. J., Garrison, R. F., McFadden, M. T., & Robinson, P. E. 2003, AJ, 126, 2048

- Gray, R. O., Corbally, C. J., Garrison, R. F., McFadden, M. T., O'Donoghue, A. A., Knox, E. R., McGahee, C. E., & Bubar, E. J. 2004, *Bulletin of the American Astronomical Society*, 36, 1488
- Gray, R. O., Corbally, C. J., Garrison, R. F., McFadden, M. T., Bubar, E. J., McGahee, C. E., O'Donoghue, A. A., & Knox, E. R. 2006, *AJ*, 132, 161
- Hambly, N.C., Henry, T.J., Subasavage, J.P., Brown, M.A., & Jao, W-C. 2004, *AJ*, 128, 437
- Hartung, M. et al. 2004, *Astronomy and Astrophysics*, 421, L17
- Hinkley, S., et al. 2007, *ApJ*, 654, 633
- Houk, N., & Cowley, A. P. 1975, “Michigan Catalog of Two-Dimensional Spectral Types for the HD Stars”, Ann Arbor: University of Michigan, Department of Astronomy, 1975
- Houk, N. 1978, Ann Arbor : Dept. of Astronomy, University of Michigan : distributed by University Microfilms International
- Houk, N. 1982, Michigan Spectral Survey, Ann Arbor, Dep. Astron., Univ. Michigan, 3 (1982), 0
- Houk, N., & Cowley, A. P. 1988, “Michigan Catalog of Two-Dimensional Spectral Types for the HD Stars, Vol. 4”, Ann Arbor: University of Michigan, Department of Astronomy
- Houk, N., & Smith-Moore, M. 1988, Michigan Spectral Survey, Ann Arbor, Dept. of Astronomy, Univ. Michigan (Vol. 4) (1988), 0
- Ida, S., & Lin, D. N. C. 2005, *ApJ*, 626, 1045
- Janson et al. 2007, *AJ*, *subm.*
- Kaisler, D., Zuckerman, B., & Becklin, E. 2003, *ASP Conference Series*, 294, 91
- Kellner et al. 2007, *submitted*
- Kenworthy, M.A., Hinz, P.M., Angel, J.R.P, Heinze, A.N., & Sivanandam, S. 2006, *Proc. SPIE*, 6272, 104
- Knapp, G. R. et al. 2004, *ApJ*, 127, 3553
- Lachaume, R., Dominik, C., Lanz, T., & Habing, H. J. 1999, *A&A*, 348, 897
- Leaton, B. R., & Pagel, B. E. J. 1960, *MNRAS*, 120, 317

- Lenzen, R. et al. 2003, Proc. SPIE, 4841, 944
- Lenzen, R., Close, L., Brandner, W., Hartung, M., & Biller, B. 2004, Proc. SPIE, 5492, 970
- Lenzen, R., Close, L., Brandner, W., Biller, B., & Hartung, M. 2005, Science with AO ESO Workshop, 46
- Li, J. Z., & Hu, J. Y. 1998, A&AS, 132, 173
- Liu, M. et al. 2005, NICI campaign science proposal
- Liu, W. et al. 2006, accepted to ApJ
- Lowrance, P. J., et al. 2005, AJ, 130, 1845
- Luhman, K.L., et al. 2006, ApJ, 649, 894
- Macintosh, B., Graham, J., Palmer, D., Doyon, R., Gavel, D., Larkin, J., Oppenheimer, B., Saddlemyer, L., Wallace, J., Bauman, B., Evans, J., Erikson, D., Morzinksi, K., Phillion, D., Poyneer, L., Sivaramakrishnan, A., Soummer, R., Thibault, S., & Veran, J.-P. 2006, Proc. SPIE, 6272, 18
- Marley, M.S., Fortney, J.J., Hubickyj, O., Bodenheimer, P., and Lissauer, J.J. 2006, astro-ph/0609739
- Marois, C., Doyon, R., Racine, R., & Nadeau, D. 2000, PASP, 112, 91
- Marois, C., Doyon, R., Racine, R., & Nadeau, D. 2002, Proc. SPIE, 4008, 788
- Marois, C. et al. 2005, PASP, 117, 745
- Marois, C., Lafrenière, D., Doyon, R., Macintosh, B., & Nadeau, D. 2006, ApJ, 641, 556
- Masciadri, E., Mundt, R., Henning, T., Alvarez, C., & Barrado y Navascues, D. 2005, ApJ, 625, 1004
- McCaughrean, M.J., Close, L.M., Scholz, R.-D., Lenzen, R., Biller, B., Brandner, W., Hartung, M., & Lodieu, N. 2004, Astronomy and Astrophysics, 413, 1029
- Metchev, S. A., & Hillenbrand, L. A. 2004, ApJ, 617, 1330
- Meyer, M. R., Edwards, S., Hinkle, K. H., & Strom, S. E. 1998, ApJ, 508, 397
- Mochnicki, S.W. et al. 2002, AJ, 124, 2868

- Montes, D., López-Santiago, J., Gálvez, M. C., Fernández-Figueroa, M. J., De Castro, E., & Cornide, M. 2001, *MNRAS*, 328, 45
- Mugrauer, M. & Neuhauser, R. 2005, *MNRAS*, 361, L15
- Nakajima, T., Oppenheimer, B.R., Kulkarni, S., Golimowski, D.A., Matthews, K., & Durrance, S.T. 1995, *Nature*, 378, 463
- Neuhauser, R., & Brandner, W. 1998, *A&A*, 330, L29
- Nielsen, E. L., Close, L. M., Guirado, J. C., Biller, B. A., Lenzen, R., Brandner, W., Hartung, M., & Lidman, C. 2005, *Astronomische Nachrichten*, 326, 1033
- Nielsen, E. L., Close, L. M., & Biller, B. A. 2006, *IAU Colloq. 200: Direct Imaging of Exoplanets: Science & Techniques*, 111
- Noyes, R. W., Weiss, N. O., & Vaughan, A. H. 1984, *ApJ*, 287, 769
- Perryman, M.A.C. et al. 1997, *ApJ*, 323, 49
- Racine, R., Walker, G.A.H., Nadeau, D., Doyon, R., & Marois, C. 1999, *PASP*, 111, 587
- Randich, S., Gratton, R., & Pallavicini, R. 1993, *A&A*, 273, 194
- Rousset, G. et al. 2003, *Proc. SPIE*, 4389, 140
- Schneider, G., Becklin, E., Close, L., Figer, D., Lloyd, J., Macintosh, B., Hines, D., Max, C., Potter, D., Rieke, M., Scoville, N., Thompson, R., Weinberg, A., & Windhorst, R. 2003, solicited by STScI in preparation for HST Cycle 12
- Sparks, W. B., & Ford, H. C. 2002, *ApJ*, 578, 543
- Sozzetti, A., et al. 2006, *A&A*, 449, 417
- Tamura, M. & Lyu, A. 2006, *IAUC 200 proceedings*
- Thatte, N. et al. 2007, *MNRAS*, submitted
- Torres, G., Stefanik, R., Latham, D., & Mazeh, T. 1995, *Astrophysical Journal*, 452, 870
- Trauger, J.T., Burrows, C., Gordon, B., Green, J.J., Lowman, A.E., Dwight, M., Niessner, A.F., Shi, F., & Wilson, D. 2004, *Proc. SPIE*, 5487, 1330
- Wichmann, R., Schmitt, J. H. M. M., & Hubrig, S. 2003, *A&A*, 400, 293

Wright, J. T., Marcy, G. W., Butler, R. P., & Vogt, S. S. 2004, *ApJS*, 152, 261

Wright, J. T., Butler, R. P., Marcy, G. W., Vogt, S. S., Fischer, D. A., Rinney, C. G., & Jones, H. R. A. 2005, *Protostars and Planets V*, 8605

Zuckerman, B., Song, I., Bessell, M. S., & Webb, R. A. 2001, *ApJ*, 562, L87

Zuckerman, B., Webb, R. A., Schwartz, M., & Becklin, E. E. 2001, *ApJ*, 549, L233

Zuckerman, B., & Song, I. 2004, *ARA&A*, 42, 685